APPLIED
COMPUTATIONAL
ELECTROMAGNETICS
SOCIETY
JOURNAL

March 2018
Vol. 33 No. 3
ISSN 1054-4887

THE APPLIED COMPUTATIONAL ELECTROMAGNETICS SOCIETY JOURNAL

Vol. 33 No. 3   March 2018

TABLE OF CONTENTS – REGULAR PAPERS

TABLE OF CONTENTS – EXPRESS PAPERS

Multi-level Fast Multipole Algorithm for 3-D Homogeneous Dielectric Objects Using MPI-CUDA on GPU Cluster

Tuan Phan, Nghia Tran, and Ozlem Kilic

Department of Electrical Engineering and Computer Science
The Catholic University of America, Washington, DC, 20064, USA
30phan@cua.edu, 16tran@cua.edu, kilic@cua.edu

Abstract — The implementation of Multi-level Fast Multipole Algorithm (MLFMA) on a 13-node Graphical Processing Unit (GPU) cluster using Message Passing Interface (MPI) and CUDA programming is presented. The performance achievements are investigated in terms of accuracy, speed up, and scalability. The experimental results demonstrate that our MLFMA implementation on GPUs is much faster than (up to 66x) that of the CPU implementation without trading off the accuracy.

Index Terms — Graphics Processing Unit (GPU), Multilevel Fast Multipole Algorithm (MLFMA).

I. INTRODUCTION

In the last two decades, many authors have been investigating solving large scale electromagnetics problems using numerical techniques such as Method of Moments (MoM), Fast Multipole Method (FMM) and Multi-level Fast Multipole Algorithm (MLFMA). Modeling large-scale objects requires large memory resources and computational time. Among these methods, the MLFMA has the least computational complexity $O(NlogN)$, while MoM and FMM have the complexity of $O(N^3)$ and $O(N^{3/2})$, respectively.

MLFMA has successfully been implemented in parallel on CPU clusters to solve up to few hundreds millions of unknowns [1]. The CPU cluster-based parallel implementation has advantages of large memory resources, but their speed is relatively slow in comparison with GPU cluster-based implementations. In the past, our group has implemented a parallel version of MLFMA on GPUs clusters to solve for perfect electric conductor (PEC) objects [2]. This paper continues our efforts to investigate the implementation of MLFMA on GPU cluster platform for solving large scale dielectric objects. The platform we employ is a 13-node GPU cluster, which utilizes NVidia Tesla M2090 GPU. An MVAPICH2 implementation of Message Passing Interface (MPI) is used for parallel programming.

In this work, a workload partitioning technique, namely group-based distribution is investigated among the 13 computing nodes. This technique is applied for the tree structure in MLFMA as will be discussed in details in the implementation section. The rest of the paper is organized as follows. An overview of MLFMA for homogeneous dielectric objects is provided in Section 2. Section 3 presents the parallel implementation of MLFMA on GPU clusters. Simulation results are discussed in Section 4, followed by the conclusions in Section 5.

II. OVERVIEW OF THE MULTILEVEL FAST MULTIPOLE ALGORITHM ON DIELECTRIC OBJECTS

In this section, we provide a brief overview to help our discussion on the parallel implementation of dielectric MLFMA, which is presented in Section III. Numerical techniques such as MoM, FMM, and MLFMA are invented to solve for the linear equation system ZI = V, where I represents the unknown currents, V depends on the incident field, and Z is the impedance matrix. For an arbitrary structure meshed with M-edges the conventional MoM requires the computation of all direct interactions among the edges (MxM), while FMM accelerates the matrix-vector product by using an approximate multiple expansion of the fields to divide structure into near and far group interaction concept [3]. MLFMA is based on FMM, but it relies on forming hierarchical groupings to render reactions with far groups more efficiently. The main idea of the grouping concept of MLFMA is shown in Fig. 1, where M edges are categorized into an N-level tree structure. For the sake of simplicity and convenience, the oct-tree structure is used for grouping in MLFMA [4].

The near interactions among edges in spatially nearby groups are computed and stored using the conventional MoM [5], while the far interactions are calculated in a group-by-group manner consisting of three stages, namely, aggregation, translation, and disaggregation.

In our previous work on FMM for a homogeneous dielectric object (permittivity ε_2, permeability μ_2)

immersed in an infinite homogeneous medium (permittivity ε_1, permeability μ_1), the basic formulas are given as:

$$Z^1_{ij,JJ} = \frac{\omega\mu k}{16\pi^2}\int d^2\hat{k}\, \boldsymbol{T}^E_{r_{im}}(\hat{k})T_L(k,\hat{k},\boldsymbol{r}_{ii'})\bullet R^E_{m'i'}(\hat{k}), \quad (1)$$

$$Z^1_{ij,MM} = \frac{\omega\varepsilon k\eta^2}{16\pi^2}\int d^2\hat{k}\, \boldsymbol{T}^E_{r_{im}}(\hat{k})T_L(k,\hat{k},\boldsymbol{r}_{ii'})\bullet R^E_{m'i'}(\hat{k}), \quad (2)$$

$$Z^1_{ij,MJ} = \frac{k\eta}{16\pi^2}\int d^2\hat{k}\, \boldsymbol{T}^{ED}_{r_{im}}{}'(\hat{k})T_L(k,\hat{k},\boldsymbol{r}_{ii'})\bullet R^E_{m'i'}(\hat{k})$$
$$= -Z^1_{ij,JM}, \quad (3)$$

where

$$T^E_{r_{im}} = \int_S (\boldsymbol{I} - \hat{k}\hat{k})\bullet f_m(\boldsymbol{r}_{im})e^{-jk\bullet r_{im}}dS, \quad (4)$$

$$T^{ED}_{r_{im}} = \int_S \hat{k}\times f_m(\boldsymbol{r}_{im})e^{-jk\bullet r_{im}}dS, \quad (5)$$

$$R^E_{r_{m'i'}} = \int_S f_{m'}(\boldsymbol{r}_{m'i'})e^{-jk\bullet r_{m'i'}}dS, \quad (6)$$

$$T_L = \sum_{l=0}^{L}(-j)^l(2l+1)h_l^{(2)}(\boldsymbol{k}\bullet\boldsymbol{r}_{ii'})P_l(\hat{\boldsymbol{k}}\bullet\boldsymbol{r}_{ii'}), \quad (7)$$

In the above equations, L denotes for multipole expansion number, $h_l^{(2)}$ identifies the second kind of Hankel function, P_l stands for Legendre polynomial of degree l terms. By the changing the sub and superscripts "1" to "2" in Equations (1) to (7), we can complete the 2N linear equations. The same idea applies for MLFMA to solve for dielectric object [6].
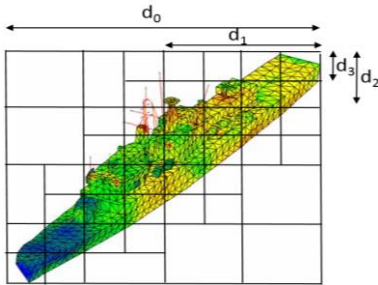
Fig. 1. MLFMA general grouping concepts.

III. GPU CLUSTER IMPLEMENTATION OF MLFMA

In this section, a detailed implementation of MLFMA is provided. The implementation is divided into three main blocks, which consist of pre-processing, processing and post-processing.

While the pre-processing and post processing processes utilize CPU, the processing are based on GPU cluster. The main purpose of the pre-processing step is to read the geometry mesh data, to set up the data structure, and to construct the oct-tree. Results from this process are transferred to the GPU memory, and the entire computation is performed on the GPU clusters. The user interested quantities such as scattered fields, radar cross section, are post-processing and handled on CPU. The processing step is the most time consuming in

the algorithm. Hence, we focus our parallel programming of MLFMA on the most computationally intensive step, i.e., the processing. The details of this process is shown in Fig. 2.
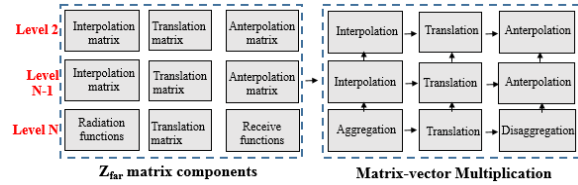
Fig. 2. A detail implementation of processing phase.

In the processing phase, the computational tasks are assigned to all computing nodes in a balanced manner such that each node holds the same amount of workload, and the inter-node communication is minimized. This is achieved by uniformly distributing the total number of groups of all levels except level 1 and 2, G, among the n computing nodes. We define this technique of data distribution among computing nodes as the group-based distribution. Two levels of parallelization are performed in this stage: among the n computing nodes using MPI library, and within the GPU per node using CUDA programming model. The CUDA thread-block model is utilized to calculate the assigned workload within a node. In this paper, only the far interactions is presented, and the near field and V vector calculation implementations can be found in [7].

The GPU cluster used for this work has 13 computing nodes. Each node has a dual 6-core 2.66 GHz Intel Xeon processor, 48 GB RAM along with one NVidia Tesla M2090 GPU running at 1.3 GHz supported with 6GB of GPU memory. The nodes are interconnected through the InfiniBand interconnection. The cluster populates CUDA v6.0 and MVAPICH2 v1.8.1 (an implementation of MPI).

A. Far interactions calculations

There are five main steps in this stage: radiation functions, receive function, interpolation, anterpolation and translation matrices. The group-based technique is performed to calculate the radiation functions, receive functions, and translation matrices.

(i) Radiation and Receive Function Calculations

The calculation of the radiation, T^E, and receive, R^E, functions for Z^{far} matrix are similar since R^E is the complex conjugate of T^E. Following the G group distribution as mentioned above, each computing node handles the calculation of K directions for G_{node} groups.

(ii) Translation Matrix Calculation

The workload for the T_L calculations is also distributed across the n nodes using the group-based

technique. In order to save memory, each CUDA block is assigned to compute one sparse row of the T_L matrix for a given direction.

(iii) Interpolation and Anterpolation Matrices

Due to the differences of sampling frequencies among the levels of the oct-tree structure, the interpolation and anterpolation are required for the aggregation and disaggregation stages. In this task, each node will handle the calculations of $K_{children/node}$ rows of the interpolation matrix $K_{children} * K_{parent}$, where $K_{children}$ and K_{parent} are the number of directions of finer and coarser level, respectively. The blocks of a maximum of 1024 threads are utilized in the CUDA kernel once it is launched. The anterpolation is simply the transpose of the interpolation. Thus, their implementations are similar.

B. Matrix-vector multiplication

The matrix-vector multiplication (MVM) method is an important technique to accelerate the computational time, which can be found in detail in [8]. An iterative method; i.e., the biconjugate gradient stabilized method (BiCGSTAB), is used to solve for the linear system. The computation of $Z_{far}I$ is shown in Fig. 3, where the unknown current vector I is distributed among the 13 nodes using the group-based technique [9].
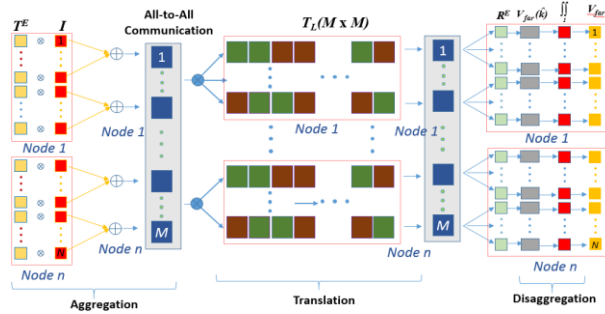
Fig. 3. The parallelization of matrix-vector multiplication for $Z_{far}I$.

First, in the aggregation stage, at level max, (N), each node computes the radiated fields for its assigned groups by multiplying the current I with the radiation functions, T^E, and accumulating within each group. Then, all-to-all communication is required to broadcast the data to all nodes. For the remaining levels (up to level 2), the radiated field is the result of multiplying interpolation matrices with radiated fields of its direct children groups.

In the translation stage, at each level (except levels 0 and l) the radiated fields for each group are calculated by multiplying the translation matrix with the radiated fields.

In the disaggregation stage, going down from level 2 to level N, the radiated fields at each group are added with the inherited fields from its parents using anterpolation. At the maximum level (N), the received fields are multiplied with their corresponding receive functions, and integrated over K directions. Then, the near components and far components of MVM are incorporated to complete the full matrix. In the end of this process, the results from all nodes are summed and updated.

IV. EXPERIMENTAL RESULTS

A. Accuracy

The accuracy of the method is verified by comparing the Radar Cross Sections (RCSs) of 9λ-diameter dielectric sphere with analytical technique, Mie scattering, and a 10λ-height by 4λ-radius dielectric cone with commercial simulation software, FEKO. In two cases, the results verify our method's accuracy, as observed in Fig. 4 and Fig. 5, respectively.
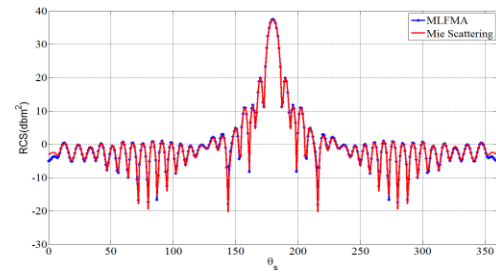
Fig. 4. RCS of a 9λ diameter dielectric sphere ($\varepsilon = 4 - 0.1i$) with 105,000 unknowns.
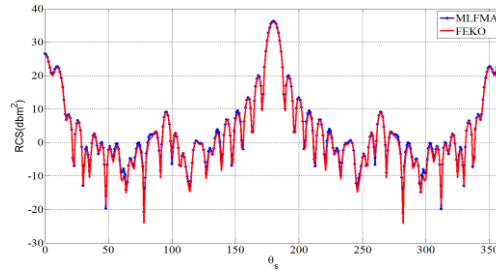
Fig. 5. RCS of 10λ height and 4λ radius dielectric cone ($\varepsilon = 4 - 0.1i$) with 109,000 unknowns.

B. Performance on GPU cluster

We conducted two experiments to investigate the speed-up, scalability using a fixed-workload model (Amdahl's Law) and maximum problem size. The speed-up is defined as the ratio of time required by multi-node GPU implementation with respect to the 8-node CPU implementation. The scalability is the normalized speed-up of multiple nodes in reference to the speed-up of 8 nodes. Finally, we fully utilized the memory available of 13 nodes to investigate the maximum number of unknowns we can handle.

In the first experiment, a 16.74 λ-diameter dielectric

sphere (320k unknowns) which requires the memory of at least 8 nodes is used. The results are evaluated in terms of speed-up and scalability. As shown in Fig. 6, the speed-up for process of matrix-vector products and matrix fill increases from 45.6 for 8 nodes to 66.4 for 13 nodes. The GPU execution time decreases as the number of nodes increases because of less workload per node.
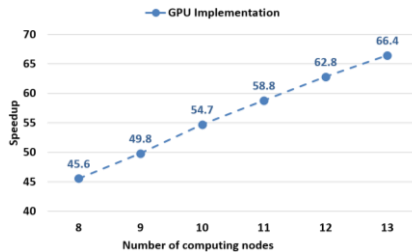
Fig. 6. Speedup analysis for the fixed-workload model (vs. 8 nodes CPU implementation, 100 iterations).

For the scalability, we keep the problem size constant and compare how the speed-up improves with increasing number of nodes, Fig. 7. It shows a good agreement between our implementation and the theoretical expectation.

In the second experiment, we try to solve for the largest problem size using the maximum memory available to us in each node. As the number of nodes increases, we increase the problem size to fully utilize the available memory. As shown in Fig. 8, we can process a maximum problem size of 439k unknowns with a speed-up of 46.
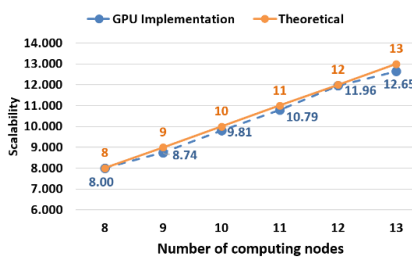
Fig. 7. Scalability analysis for the fixed-workload model.
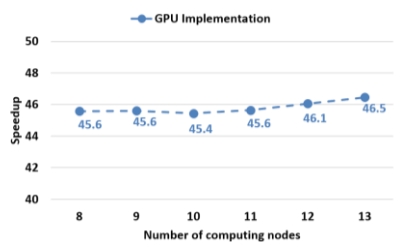
Fig. 8. Speed-up analysis for increasing number of nodes along with problem size increases.

V. CONCLUSION

In this paper,MLFMA for homogeneous dielectric objects has bee implemented using GPU clusters. Our 13-node GPU cluster is able to solve 426k unknowns utilizing the available on-board GPU memory. It demonstrates that the GPU implementation is much faster than CPU implementation while keeping a same degree of accuracy.

REFERENCES

[1]   O. Ergul and L. Gurel, "Efficient parallelization of the multilevel fast multipole algorithm for the solution of large-scale scattering problems*," IEEE Trans. Antennas Propag.*, vol. 56, no. 8, pp. 2335-2345, August 2008.

[2]   N. Tran and O. Kilic, "Parallel implementations of multilevel fast multipole algorithm on graphical processing unit cluster for large-scale electromagnetics objects," *ACES Express Journal*, vol. 1, no. 4, April 2016.

[3]   R. Coifman, V. Rokhlin, and S. Wandzura, "The fast multipole method for the wave equation: A pedestrian prescription," *IEEE Antennas Propagat. Mag.*, vol. 35, no. 3, pp. 7-12, June 1993.

[4]   H. Samet, *An Overview of Quadtrees, Octrees, and Related Hierarchical Data Structures*. NATO ASI Series, vol. F40, Springer-Verlag Berlin Heidelberg, 1988.

[5]   S. M. Rao, D. R. Wilton, and A. W. Glisson, "Electromagnetic scattering by surfaces of arbitrary shape," *IEEE Trans. Antennas Propag.*, vol. AP-30, no. 3. pp. 409-418, May 1982.

[6]   J.-Y. Li and L.-W. Li, "Characterizing scattering by 3-D arbitrarily shaped homogeneous dielectric objects using fast multipole method," *IEEE Antennas and Wireless Propagation Letters*, vol. 3, 2004.

[7]   Q. M. Nguyen, V. Dang, O. Kilic, and E. El-Araby, "Parallelizing fast multipole method for large-scale electromagnetic problems using GPU clusters," *Antennas and Wireless Propagation Letters, IEEE*, vol. 12, pp. 868-871, 2013.

[8]   V. Dang, Q. Nguyen, and O. Kilic, "Fast multipole method for large-scale electromagnetic scattering problems on GPU cluster and FPGA-accelerated platforms," *Applied Computational Electromagnetics Society Journal*, vol. 28, no. 12, 2013.

[9]   V. Dang, Q. M. Nguyen, and O. Kilic, "GPU cluster implementation of FMM-FFT for large-scale electromagnetic problems," *IEEE Antennas and Wireless Propagation Letters*, vol. 13, 2014.

A Substrate Integrated Waveguide Based Antipodal Linear Tapered Slot Antenna for 60 GHz Wireless Communications

Nishesh Tiwari and Thipparaju R. Rao

Department of Telecommunication Engineering
SRM University, Chennai-603203, India
nitizaz@gmail.com, ramaraot@outlook.com

Abstract ─ Antipodal linear tapered slot antenna (ALTSA) for 60 GHz communications is presented in this paper. To obtain a high gain, dielectric loading in addition to the corrugation structure is applied to the ALTSA. The use of substrate integrated waveguide (SIW) technology allows a highly efficient, compact and low cost planar design. The antenna is designed and simulated in an electromagnetic field simulation tool. To validate the proposed design, a prototype has been fabricated and measured. The simulated results agree well with the measured values, which validates the proposed design. The radiation efficiency is observed to be 92%. The antenna has a gain of 18.7 ± 0.5 dBi. The return loss is better than 10 dB over the 60 GHz band (57 GHz – 64 GHz).

Index Terms ─ Antipodal linear tapered slot antenna, dielectric loading, high gain, substrate integrated waveguide, 60 GHz.

I. INTRODUCTION

The ever-growing demand of high speed communication has made the unlicensed 60 GHz band (57 GHz–64 GHz) a smart option for wireless communication allowing transfer of uncompressed data, voice and video at the speed of multi gigabit per second (multi-Gbps) [1]. At millimeter wave frequency band, the losses in the planar microstrip circuit is high. Therefore, this requires more efficient technology like the substrate integrated waveguide (SIW) to be used, which has positive traits of traditional rectangular waveguide such as low loss, high quality factor, complete shielding and capability of handling high power along with the advantage of low cost and planar circuit design [2]. 60 GHz band also suffers from attenuation due to atmospheric absorption. This requires the use of high gain antennas to negate the losses. Tapered slot antennas (TSA) are famous for their high gain and wide bandwidth [3]. TSA with corrugation structure have been used for reducing the width of the antenna while minimizing any significant degradation in

radiation pattern [3]. In [4], Shrivastava et al. have designed corrugated antipodal linear tapered slot antenna (ALTSA) with rectangular corrugation for 60 GHz band having the gain of 16 dBi at 60 GHz. Corrugation also increases gain and reduces side lobe level. Further, dielectric loading is also known for enhancement of antenna gain. By placing the dielectric slab in front of the antenna its gain can be increased. The dielectric slab in this case acts as a guiding structure [5] and enhances the gain of antenna. In [5], Ghassemi et al. have developed a high gain ALTSA array with SIW horn structure as the feed. Rectangular dielectric loading has been used to increase the gain of a non-corrugated ALTSA. In [5], the gain of single ALTSA is 14.25 dBi at 84 GHz and 1x4 ALTSA array is 19 ± 1 dBi. In [6], Wang et al. have applied rectangle shaped dielectric loading structure to a planar SIW horn antenna and achieved a gain of 9.7 dBi at 27 GHz. In [7], Mohamed et al. have presented an ALTSA with diamond slot dielectric loading structure. The antenna has a gain of 16.2 dBi with a wide impedance bandwidth. In [8], Ramesh et al. have designed an exponentially tapered slot antenna (ETSA) with elliptical dielectric loading structure, which has a gain of 11.4 dBi at 60 GHz.

In this paper, instead of conventional elliptical shape, a rectangle with semicircular top shaped dielectric structure is used on a corrugated ALTSA to obtain a high gain antenna in the 60 GHz band. The antenna is designed and simulated in Ansys HFSS software.

II. ANTENNA DESIGN

The antenna is designed on Rogers RT/Duroid 5880 substrate which has dielectric constant of 2.2, loss tangent of 0.0009 and thickness of 0.254 mm. For proper design of SIW, the diameter of via holes and the space between the vias should be chosen as per (1) and (2) respectively:

$$D_{via} < \frac{\lambda_g}{5}, \qquad (1)$$

$$S \leq 2D_{via}, \qquad (2)$$

where λ_g is the guided wavelength, D_{via} is the diameter of the via and S is the space between the vias. The

effective width of the waveguide is given by (3) [2]:

$$W_{eff} = W_{siw} - 1.08 \frac{D_{via}^2}{S} + 0.1 \frac{D_{via}^2}{W_{siw}}, \qquad (3)$$

where W_{eff} is the effective width, W_{siw} is the width of the SIW. The performance of TSA is sensitive to the thickness t and the dielectric constant ε_r. Hence, a factor $f_{substrate}$ is defined for efficient performance of TSA as $f_{substrate} = t(\sqrt{\varepsilon_r} - 1)/\lambda_0$ [3]. For good performance of tapered slot antenna, the substrate thickness should satisfy $0.005 \leq f_{substrate} \leq 0.03$. In this design we have chosen the substrate thickness of 0.254 mm such that $f_{substrate}$ is 0.024. ALTSA is generally designed with trial and error method. The width of the ALTSA is kept greater than 2λ [5]. The length of the flares is increased gradually until the optimum gain is achieved. Generally, the length varies from 3λ - 8λ to achieve the optimum gain. In this work, the optimum gain is observed when the length of the flares is 5λ. Firstly, the plain ALTSA is designed. Then corrugation is applied to the outer edges of the flares. Finally, a dielectric slab is added on top of the corrugated ALTSA to form the dielectric loaded ALTSA. The plain ALTSA (ALTSA-P), corrugated ALTSA (ALTSA-C) and corrugated ALTSA with dielectric loading (ALTSA-DL) are designed and simulated. Figure 1 shows the schematic of ALTSA-DL where L1 = 11.95 mm, L2 = 10.5 mm, L3 = 25 mm, L4 = 15 mm, L5 = 0.4 mm, W1 = 1.59 mm, W2 = 2.69 mm, W3 = 10.1 mm, W4 = W5 = 0.2 mm, r = 5.05 mm, V = 0.78 mm, D_{via} = 0.4 mm, S = 0.7 mm.
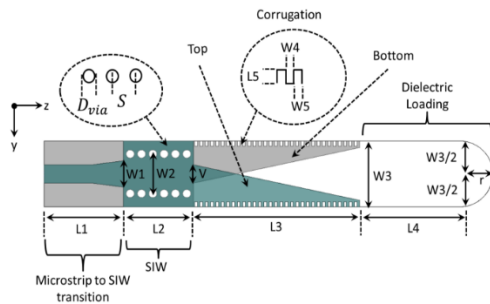
Fig. 1. ALTSA-DL schematic.

The structure of the dielectric load used in antenna has an impact on its gain. In this work, instead of a conventional elliptical dielectric loading structure, a rectangle with semi-circular top shaped design for dielectric loading is proposed. During simulation it is observed that rectangle with semicircular top shaped dielectric loading gives higher gain than conventional elliptical dielectric loading structure. The maximum difference in gain is observed to be around 0.76 dBi.

III. SIMULATION AND MEASUREMENT

Figure 2 shows the E-field distribution. The simulated gain and return loss of ALTSA are shown in Fig. 3. It is observed that return loss for ALTSA-P,

ALTSA-C and ALTSA-DL are all better than 10 dB in the 60 GHz band (57-64 GHz). Also, it is observed that the return loss changes as corrugation and dielectric loading structure is added to the antenna. At 60 GHz, the ALTSA-DL has return loss better than 23 dB. Similarly, from Fig. 3 it is also observed that the gain of ALTSA-P, ALTSA-C and ALTSA-DL is 14.4 ± 0.3 dBi, 17.1 ± 0.3 dBi and 18.8 ± 0.6 dBi respectively. The simulated E-plane radiation pattern is shown in Fig. 4. In the E-plane the 3-dB beamwidth of ALTSA-P, ALTSA-C and ALTSA-DL is observed to be 22.6°, 19.5° and 17.5° respectively. Also, the side lobe level of ALTSA-P, ALTSA-C and ALTSA-DL in E-plane is observed to be at -13 dB, -15 dB and -17 dB respectively. Similarly, the cross polarization level of ALTSA-P, ALTSA-C and ALTSA-DL is observed to be better than 14 dB, 21 dB and 22 dB respectively.
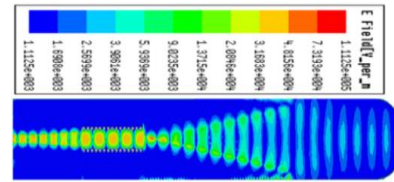
Fig. 2. E-field distribution in ALTSA-DL.
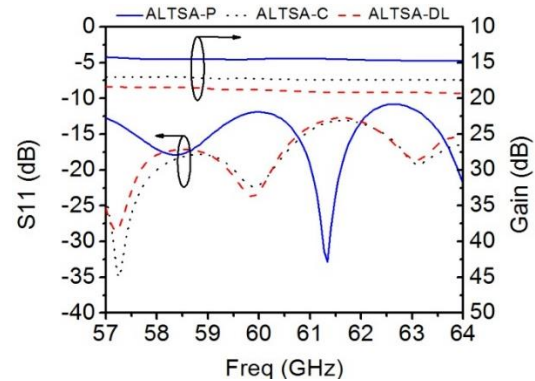
Fig. 3. Simulated return loss and gain.
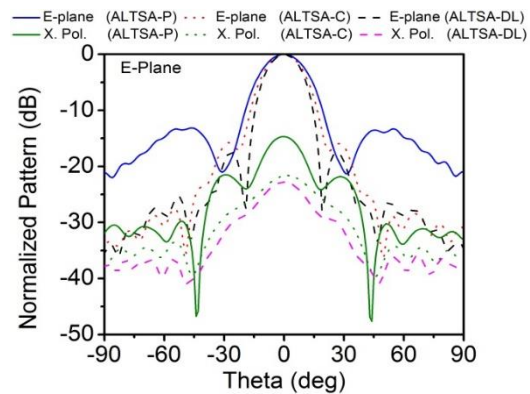
Fig. 4. Simulated E-plane radiation pattern at 60 GHz.

The simulated H-plane radiation pattern is shown in Fig. 5. The 3-dB beamwidth in the H-plane of ATLSA-P, ALTSA-C and ALTSA-DL is observed to be 29.5°, 33.1° and 25.2° respectively. Further, the side lobe level of ALTSA-P, ALTSA-C and ALTSA-DL in H-plane is observed to be -13 dB, -12 dB and -15dB respectively. Also, the cross polarization level of ALTSA-P, ALTSA-C and ALTSA-DL is seen to be better than 14 dB, 21 dB and 22 dB respectively. It is noted that, though with corrugation the E-plane beamwidth decreases but the beamwidth increases in H-plane. Overall it is found that ALTSA-DL has the narrowest beamwidth, lowest side lobe level and better cross polarization in both E- and H-planes. Therefore ALTSA-DL is found to have the best performance. Hence, ALTSA-DL is fabricated and its performance parameters are measured to validate the design.
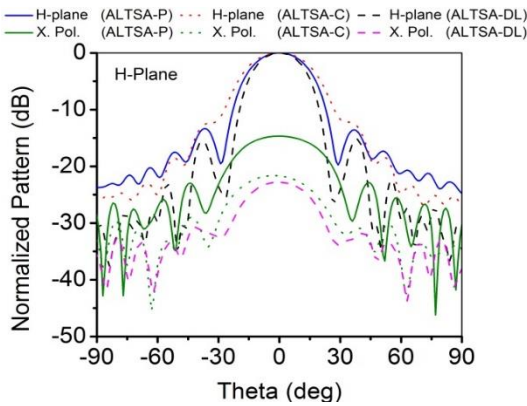
Fig. 5. Simulated H-plane radiation pattern at 60 GHz.

Figure 6 shows the fabricated ALTSA-DL prototype. The dimension of ALTSA-DL is 67.5 mm x 10.1 mm. It is compact in size and light weight. It is fabricated using the low cost printed circuit board (PCB) technology. The S11 parameters and gain of ALTSA-DL are measured utilizing MVNA-8-350 with probe station. The radiation pattern measurement has been performed in a far-field anechoic chamber.
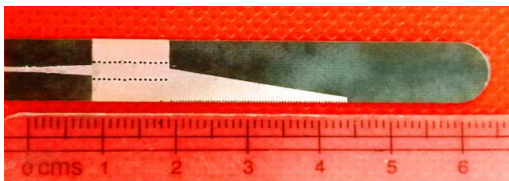
Fig. 6. Fabricated ALTSA-DL.

Figure 7 shows the measured gain and return loss of the ALTSA-DL. From Fig. 7, it is observed that measured gain of ALTSA-DL is 18.7± 0.5 dB over the entire 60 GHz band (57-64 GHz). The antenna gain is almost flat over the entire bandwidth. Similarly, measured return loss

is observed to be better than 12 dB over the 60 GHz band. At 60 GHz, return loss is better than 22 dB. The discrepancy observed in the measured return loss with slight frequency shift can be attributed to the fabrication tolerances. Figure 8 shows the measured E-plane radiation pattern of ALTSA-DL at 60 GHz. The measured 3-dB beamwidth of ALTSA-DL in E-plane is 17° and the side lobe level is at -17 dB, which is similar to the values obtained from simulation. Similarly, Fig. 9 shows the measured H-plane radiation pattern of ALTSA-DL at 60 GHz. The measured 3-dB beamwidth of ALTSA-DL in H-plane is observed to be 22.7° and the side lobe level is at -15.7 dB. Further, it is seen that the simulated and measured radiation patterns are in good agreement in both E-plane and H-plane. Also, the radiation efficiency is observed to be 92%.

Table 1 lists the comparison with other SIW based antennas having different dielectric loading structures such as rectangle in [6], elliptical in [8] etc. It is observed that though the proposed antenna has less impedance bandwidth as compared to [7], its gain is better as compared to other antennas. Further, its impedance bandwidth covers 57-64 GHz, which is adequate for multi-Gbps communication at 60 GHz.
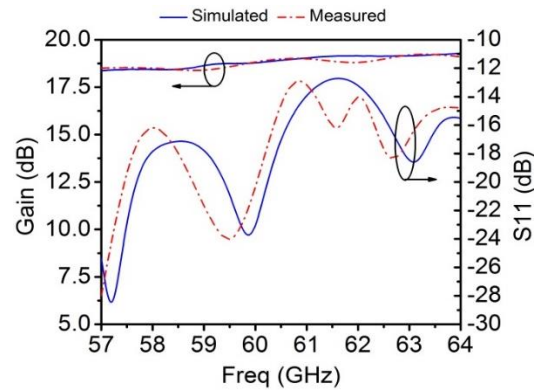
Fig. 7. Simulated and measured return loss and gain of ALTSA-DL.
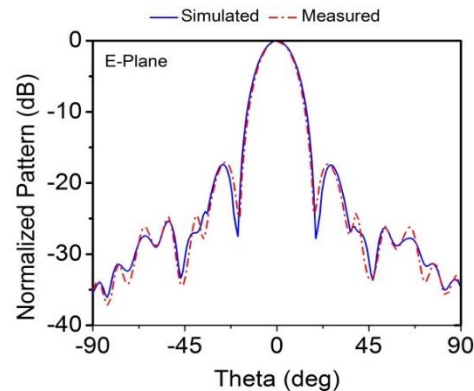
Fig. 8. Simulated and measured E-plane radiation pattern of ALTSA-DL at 60 GHz.
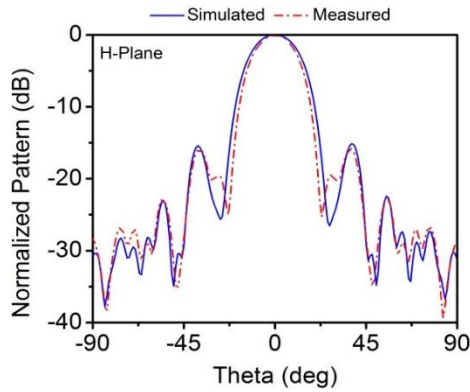
Fig. 9. Simulated and measured H-plane radiation pattern of ALTSA-DL at 60 GHz.

Table 1: Comparison with other antennas

Parameter	[6]	[7]	[8]	This Work
Antenna	Horn	ALTSA	ETSA	ALTSA
Dielectric loading structure	Rect.	Diamond slot	Ellip.	Rect. with semicircular top
Gain (dBi)	9.7	16.2	11.4	18.8
Impedance bandwidth	5.5%	33.3%	5.5%	11.6%
Operation frequency (GHz)	27	60	60	60

IV. CONCLUSION

A high gain ALTSA with dielectric loading is presented in this paper. The antenna has high gain, compact size, light weight, ease of fabrication using PCB technology and it is also fit for mass production. Hence, the proposed antenna is suitable for high speed communication in 60 GHz band.

ACKNOWLEDGMENT

REFERENCES

[1] P. Smulders, "Exploiting the 60 GHz band for local wireless multimedia access: Prospects and future directions," *IEEE Communication Magazine*, vol. 40, pp. 140-147, 2002.

[2] M. Bozzi, A. Georgiadis, and K. Wu, "Review of substrate-integrated waveguide circuits and antennas," *IET Microwaves, Antennas & Propagation*, vol. 5, pp. 909-920, 2011.

[3] T. Djerafi and K. Wu, "Corrugated substrate integrated waveguide antipodal linearly tapered slot antenna array fed by quasi-triangular power divider," *PIER C*, vol. 26, pp. 139-151, 2012.

[4] P. Shrivastava, D. Chandra, N. Tiwari, and T. R. Rao, "Investigations on corrugation issues in SIW based antipodal linear tapered slot antenna for wireless networks at 60 GHz," *ACES Journal*, vol. 28, pp. 960-967, 2013.

[5] N. Ghassemi and K. Wu, "Planar high-gain dielectric-loaded antipodal linearly tapered slot antenna for E- and W-band gigabyte point-to-point wireless services," *IEEE Transactions on Antennas and Propagation*, vol. 61, pp. 1747-1755, 2013.

[6] H. Wang, D. G. Fang, B. Zhang, and W. Q. Che, "Dielectric loaded substrate integrated waveguide (SIW) H-plane horn antennas," *IEEE Transactions on Antennas and Propagation*, vol. 58, pp. 640-647, 2010.

[7] I. Mohamed and A. Sebak, "Dielectric loaded antipodal linearly tapered slot antenna for 60 GHz applications," *Global Symposium on Millimeter Waves*, pp. 1-2, 2015.

[8] S. Ramesh and T. R. Rao, "Planar high gain dielectric loaded exponentially tapered slot antenna for millimeter wave wireless communications," *Wireless Personal Communications*, vol. 84, pp. 3179-3192, 2015.

Installed Antenna Performance in Airborne Radomes of Different Profiles

Ana Vukovic, Phillip Sewell, Xuesong Meng, and Trevor M. Benson

George Green Institute for Electromagnetics Research, Department of Electrical and Electronic Engineering
University of Nottingham, Nottingham, NG7 2RD, UK
ana.vukovic@nottingham.ac.uk, xuesong.meng@nottingham.ac.uk, trevor.benson@nottingham.ac.uk,
phillip.sewell@nottingham.ac.uk

Abstract ─ In this paper, broadband interactions between an antenna and a radome are modelled using a full wave numerical solver. By accurately describing both the antenna and the radome geometry with a single numerical method, a comprehensive prediction of the performance of the coupled antenna and radome installation is provided. The paper compares how different airborne dielectric radome profiles affect the antenna performance, predicting effects not seen in uncoupled simulations.

Index Terms ─ Airborne radome, installed antenna, unstructured transmission line modelling method.

I. INTRODUCTION

Airborne radomes are weatherproof enclosures that protect antennas from the physical environment but are intended to have minimal impact on antenna performance. In practice, the aerodynamic requirements on a radome's profile compromises their benign nature for installed antenna performance; this typically manifests itself as an increase in the sidelobe level of the antenna radiation pattern and as a boresight error [1]. This is particularly true in cases where the antenna is installed close to the radome surface. In such scenarios, a better understanding of antenna-radome interactions is necessary for accurate predictions of deployed antenna performance.

Over the last decade, rapid progress in computational power and advances in distributed processing, mean that a number of numerical techniques are ever more capable of tackling larger and complex problems. Notwithstanding the advances in modelling capability, it is notable that the analysis of the electromagnetic interactions between antennas and radomes is still performed in a "decoupled" fashion, even for moderately sized problems, due to the multiscale nature of the antenna and the radome geometry [1, 2]. One common approach is to replace the intricate detail of the antenna geometry by a 3D surface of equivalent electric and magnetic currents [1]. Alternatively, the radiating fields from the antenna are computed without the radome and subsequent evaluation of the effect of the radome on the radiation pattern is performed using these fields as an excitation [1, 2]. In both approaches, decoupling the antenna from the radome means that their mutual interactions are not fully taken into account in the design and simulation cycle. It is immediately obvious that, in order to take full account of these interactions, a flexible, accurate and efficient broadband solver that can efficiently deal with the multiscale features and complex geometries of the problem is required.

In this paper we report on the application of the numerical time-domain Transmission Line Modelling (TLM) method to the fully-coupled modelling of the moderate size problem posed by radome-antenna interactions. Both the antenna and the radome are discretized within a single numerical method based upon an unstructured tetrahedral mesh, referred to as the Unstructured TLM (UTLM) method. The TLM method exploits the analogy between solutions of the 3D Maxwell's equations for electromagnetic fields and voltages and currents on an interconnected network of transmission lines to identify an explicit time stepping algorithm for the electromagnetic fields. Development of the TLM method for use with unstructured tetrahedral meshes was first reported in [3, 4] and has since been fully characterized. Unlike the finite difference and finite element time domain (FDTD, FETD) methods, the UTLM method is unconditionally stable, with stability strictly provable a priori on cell by cell basis. Late time instability is never observed and the explicit nature of the algorithm is highly efficient, without for example, introducing approaches such as mass lumping. TLM time stepping algorithms exhibit a high degree of concurrency, and hence, parallelize well on many-core processors systems. Use of tetrahedral meshes eliminates the numerical noise due to the staircase approximations to geometry typically found in the simplistic Cartesian TLM and FDTD methods. Moreover, smoother representations of curved geometrical boundaries and the inherent availability of graded meshes that permit efficient discretization of subwavelength features in large computational domains are also advantageous. The latter can be facilitated by either using a purely tetrahedral mesh, or more practically, by hybridizing

computationally efficient cubic grids and tetrahedral meshes, e.g., [5].

In this paper, antenna-radome interactions are modelled in a fully coupled manner using the UTLM method. A single broadband Vivaldi antenna enclosed in a monolithic dielectric radome of moderate size is selected as the test case. Besides the discretization, the UTLM method makes no other approximation and as long as a sufficiently fine mesh is used to discretize the whole problem, we can be assured that all physical interactions are accounted for. The open end of the dielectric radome is mounted on a perfectly conducting surface consistent with practical airborne installations. In order to separate the effect of this mounting plate and the radome's profile, the effect of the presence of just this mounting plate on the antenna's performance is investigated before the radome itself is added to the model. Spherical, spherically blunted cone and two types of superspheroidal radomes are considered, and antenna-radome interactions are assessed in terms of the return loss, S_{11}, and the radiation patterns of the installed antenna. The paper is structured as follows. In the next section the antenna geometry mounted on just the conducting plate is described and modelled. Section III then assesses how different radome profiles affect the antenna's performance, and Section IV summarizes the main conclusions of the paper.

II. ANTENNA ON THE RADOME MOUNTING PLATE

In this section, the performance of the Vivaldi antenna described in [6] mounted on a moderate size conducting plate is described. The slot line is printed on a substrate of dielectric constant $\varepsilon_{rs}=3$ and is flared to provide a smooth impedance transition between the coaxial feed and free space. The half width of the slot line varies with distance as $w(z) = 0.25e^{0.0797z}$ reaching 20 mm at the wider end. A balun is realized as a void in the flared metallic region of radius 2.5 mm. The height, width and thickness of the dielectric substrate are 55 mm, 40 mm and 1.5 mm respectively. The perfectly conducting plate is cylindrical with radius 2 m and thickness 7 mm. The coaxial feed, designed to have a characteristic impedance of 50 Ω, has inner and outer radius of 1 mm and 3.495 mm, and dielectric constant of $\varepsilon_{rc} =2.25$. The problem space is surrounded by a fictitious surface of dimensions 4.8 m x 4.6 m x 6.2 m to both terminate the space with a free space radiation boundary condition and on which to capture the radiation fields. The antenna is excited with the TEM mode of the coaxial feed modulated by a time envelope to provide a center frequency of 3.2 GHz [6] and a bandwidth spanning 1.5 to 4.5 GHz.

An example of the antenna and radome mounting plate geometry is shown in Fig. 1 and the complete geometry with a radome is shown in the inset of the Fig.

1. The whole problem is meshed with a 5 mm cubic mesh to sample the free space region [6] in conjunction with a high quality tetrahedral mesh to capture the detailed geometry. Specifically, the surfaces of, and the space around, the antenna and feed cable shown in Fig. 1, are sampled by triangular and tetrahedral cells characterized by the figure of merit Q=2. (Cell Q is defined as the ratio between the circumradius to the minimum edge length of the cell and generally values less than 5 correspond to nicely shaped cells yielding good spatial sampling [7]).
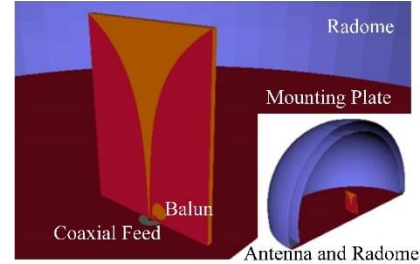
Fig. 1. Antenna on the radome mounting plate and antenna inside a radome in the inset of the figure.

Figure 2 presents S_{11} parameter for the antenna mounted on just the perfectly conducting plate. To assess the impact of mesh dispersion errors and sensitivity to the meshing in general, the simulation was also repeated using the mesh obtained when a *ghost* spherical half-wave dielectric radome of thickness of 24.2 mm, but of relative permittivity set to $\varepsilon_r=1$, is present. Physically, the radome is not electromagnetically present, but its geometry is still imprinted on the mesh. Finally, a spherical half-wave dielectric radome of permittivity $\varepsilon_r=4.2$ and wall thickness of 24.4 mm, designed to operate at 3 GHz was introduced. Figure 2 shows that there is no difference between the performance of the antenna on the just mounting plate, and with the *ghost* radome in place over the operating range, indicating no discernable sensitivity to the meshing. Moreover, this result agrees very well with that already reported in [6]. However, when for the first time, a fully coupled simulation is performed in the presence of the dielectric radome, it can be seen that S_{11} deteriorates over the operating range due to reflections form the radome. For reference, the computations simulated a total of 0.02 μs using a time step of Δt=0.01ps on 25 processor cores of a commodity cluster and required ~5.5 h to complete.

Figures 3 (a, b) compares the radiation patterns in the H- and E-plane for all three cases. Figure 3 (a) also shows the coordinate planes and the azimuthal H-plane denoted by angle ϕ and the elevation E-plane denoted by angle θ. Figure 3 shows that the radiation patterns for the antenna just on the mounting plate and with the *ghost* radome are identical, whereas the presence of the dielectric spherical radome causes stronger rippling in

the main beam of the H-plane pattern (ϕ=270 deg) and increased radiation in the sidelobe (θ=90 deg), as shown in Fig. 3 (a). The E-plane radiation pattern of the dielectric spherical radome shows slightly lower directivity compared to the antenna just on the mounting plate.
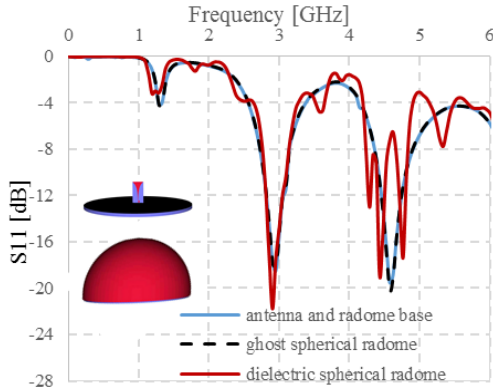
Fig. 2. S_{11} for the antenna on the mounting plate, with the *ghost* spherical radome and the dielectric spherical radome with ε_r=4.2.

(a)

(b)
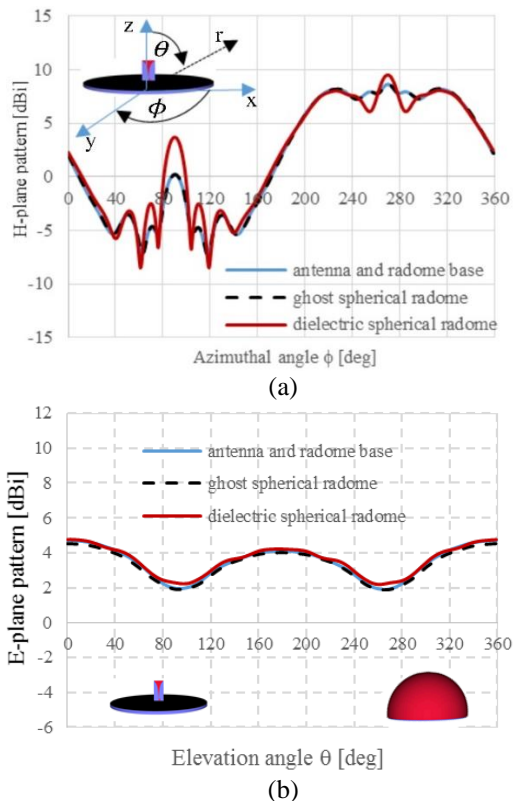
Fig. 3. (a) H-plane pattern and (b) E-plane radiation pattern for antenna on the radome base, with *ghost* spherical radome and the dielectric spherical radome.

III. IMPACT OF DIFFERENT RADOME PROFILES ON ANTENNA PERFORMANCE

In this section, the performance of the Vivaldi antenna installed in several different radomes is analyzed and compared with the case of antenna mounted on the radome base, i.e., without a radome. Illustrative aerodynamic radome profiles are chosen, namely, a spherically blunted cone and two superspheroidal profiles. In all cases, the radome's base radius and length are fixed to be R=2 m and L=2.2 m respectively. In all cases, the half-wave monolithic radome is made of a glass composite of thickness 24.4 mm and dielectric constant ε_r=4.2, which is designed to operate at 3 GHz. Radome losses are neglected. The cone profile radome is blunted by a sphere of radius 0.1 m. The superspheroidal radomes are described by the equation $x^2 + y^2 = \left(\frac{2R}{L}\right)^2 (L^p - z^p)^{2/p}$, where the coordinate z is defined along the axis of the radome, and parameter p defines the particular profile; p=1.449 and p=1.161 give the ogive and superspheroidal profiles of [2] respectively. All simulations were performed with the same meshing and run time parameters given in Section II.

Figure 4 assesses S_{11} in the operating range for the antenna installed in three different airborne radomes. The radome profiles are also given in Fig. 4. Figure 4 shows that reflections from the superspheroidal radomes tend to shift the operating frequency of the antenna and to narrow the antenna's passband. The spherically blunted cone has the least impact on S_{11} in the passband and gives the most similar behavior to the antenna performance without a radome.

Figures 5 (a, b) compares the antenna radiation patterns for the H-plane and E-plane for each radome. Figure 5 (a) shows that the superspheroid with p=1.161 causes the highest deterioration in the main lobe of the H-plane radiation pattern (ϕ=270 deg). The ogive radome (p=1.449) has reduced the directivity of the main beam of antenna (ϕ=270 deg). The spherically blunted radome has the radiation pattern most similar to the antenna with no radome. All radomes cause the slight increase in the side lobe (ϕ=90 deg). Figure 5 (b) shows that in the E-plane, the superspheroid with p=1.161 has significantly increased the directivity of antenna whilst the ogive radome (p=1.449) has decreased the directivity in the E-plane. Again, the spherically blunted radome has the E-plane pattern most similar to the antenna with no radome.

Our analysis of the effect that different superspheroidal radome profiles have on the radiation pattern of the antenna are very different from those in [2] that reported only very minor differences in sidelobes of the antenna radiation. This is, we believe, due to the "decoupled" approach employed in [2].
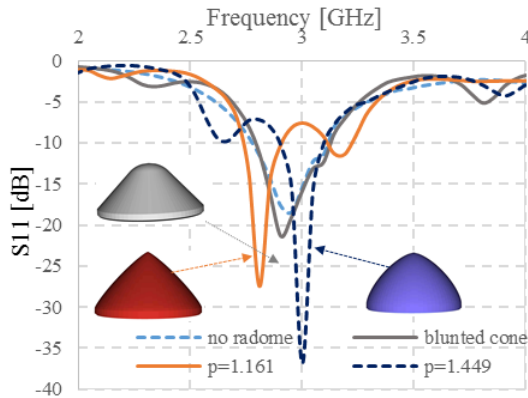
Fig. 4. Comparison of antenna S_{11} parameter in the presence of different radome profiles.

(a)

(b)
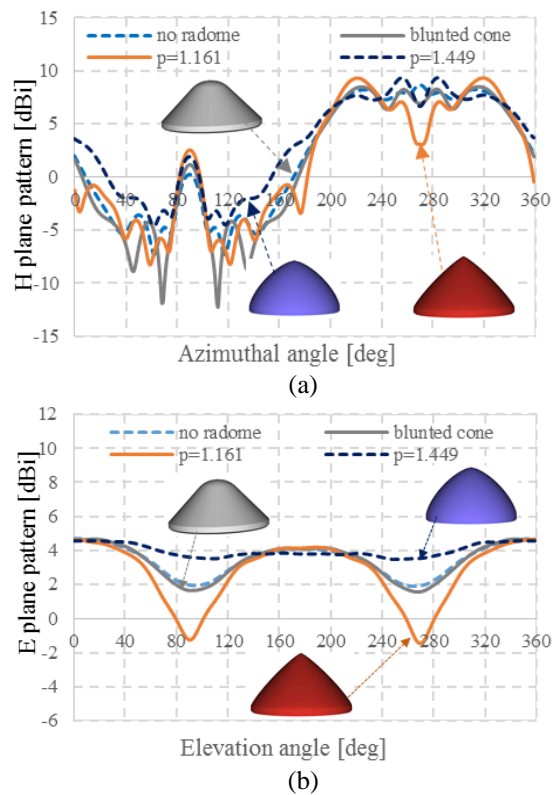
Fig. 5. Comparison of the antenna radiation pattern in the presence of different radomes for: (a) H-plane and (b) E-plane.

IV. CONCLUSION

The paper analyses broadband interactions between antennas installed in airborne radomes in a fully coupled manner by directly sampling both the antenna and the radome geometry using a single numerical method. In order to isolate the effect of the radome, the antenna's performance is first modelled in the presence of just the radome base. Two different superspheroidal radomes and the spherically blunted cone are then introduced and their impact on the antenna's performance assessed. The paper shows that a spherically blunted cone has the least influence on antenna's performance and that superspheroids can significantly change the antennas performance and need to be designed with care.

REFERENCES

[1] R. U. Nair and R. M. Jha, "Electromagnetic design and performance analysis of airborne radomes: Trends and perspectives," *IEEE Antennas and Prop. Magazine*, vol. 56, pp. 276-298, 2014.

[2] W.-J. Zhao, L.-W. Li, and Y.-B. Gan, "Efficient analysis of antenna radiation in the presence of airborne dielectric radomes of arbitrary shape," *IEEE Trans. Antennas and Prop*., vol. 53, pp. 442-448, 2005.

[3] P. Sewell, T. M. Benson, C. Christopoulos, D. W. P. Thomas, A. Vukovic, and J. G. Wykes, "Transmission line modeling (TLM) based upon unstructured tetrahedral meshes," *IEEE Trans. Microwave Theory and Tech*., vol. 53, pp. 1919-1928, 2005.

[4] P. Sewell, T. M. Benson, C. Christopoulos, D. W. P. Thomas, A. Vukovic, and J. G. Wykes, "Implicit element clustering for tetrahedral transmission-line modeling (TLM)," *IEEE Trans. Microw. Theory Tech.*, vol. 57, no. 6, pp. 2005-2014, June 2009.

[5] P. Sewell, J. G. Wykes, T. M. Benson, C. Christopoulos, D. W. P. Thomas, and A. Vukovic, "Multi-grid interface in computational electro-magnetics," *Electron. Lett*., vol. 40, pp. 162-163, 2004.

[6] A. E. Yilmaz, Z. Lou, E. Michielssen, and J. M. Jin, "A single boundary implicit and FFT-accelerated time-domain finite element-boundary integral solver," *IEEE Trans. Antennas and Propagat*., vol. 55, pp. 1382-1397, 2007.

[7] J. Shewchuk, Lecture notes on Delaunay Mesh Generation. https://people.eecs.berkeley.edu/~jrs/meshpapers/delnotes.pdf

A Compact Fractal Monopole Antenna with Defected Ground Structure for Wideband Communication

Ankan Bhattacharya [1*], Bappadittya Roy [1], Santosh K. Chowdhury [2], and Anup K. Bhattacharjee [1]

[1] Department of Electronics and Communication Engineering
National Institute of Technology, Durgapur-713209, India
*bhattacharya.ankan1987@gmail.com

[2] Department of Electronics and Telecommunication Engineering
Jadavpur University, Kolkata-700032, India

Abstract ─ A compact fractal monopole antenna with defected ground structure has been investigated in this paper. A wide bandwidth of 3.13 GHz (3.42 GHz to 6.55 GHz) has been obtained, which covers the IEEE 802.11 WLAN bands (5.2 GHz and 5.8 GHz) and WiMAX bands (3.5 GHz and 5.5 GHz). The dimension of the structure is 14.50 X 27.25 mm^2 covering an area of only 395.125 mm^2. The realized antenna gain is ≥ 2 dBi at the frequencies of interest. The compactness of the proposed structure and the simplicity of design makes it easy to be fabricated and incorporated in devices suited for wireless communication purpose.

Index Terms ─ Defected ground structure, fractal geometry, monopole antenna, wideband communication

I. INTRODUCTION

With the advent of portable mobile devices, there is a huge need for compact, low-profile patch antennas for space conservation and also for wideband communication purpose. From literature survey, it has been found that though several wideband antennas have been proposed for wideband applications particularly for WLAN and WiMAX microwave frequency bands; there still exists an issue regarding compactness in shape and size and also in realized gain of the antennas. A dual band antenna with fractal based ground plane has been proposed in [1]. The dimension of the structure is almost equal to 104 X 30 mm^2. A perturbed Sierpinski carpet antenna with CPW feed for IEEE 802.11 a/b WLAN application has been presented in [2]. The dimension of the antenna is 45 X 67.8 mm^2. A microstrip line fed printed wide slot antenna has been investigated in [3]. The antenna dimension is 70 X 70 mm^2. A broadband circularly polarized Spidron fractal slot antenna has been presented in [4]. The dimension of the proposed structure is 40 X 40 mm^2. A wideband fractal antenna with combination of fractal geometries has been presented in [5] for WLAN and WiMAX applications. The dimension of the structure is 25 X 66 mm^2. Similar types of investigations have been studied in [6] and [7], but in each case there arises an issue regarding the compactness of the proposed antenna structure. In this article, a compact fractal monopole antenna with defected ground structure has been investigated. A wide bandwidth of 3.13 GHz (3.42 GHz to 6.55 GHz) has been obtained, which covers the IEEE 802.11 WLAN bands (5.2 GHz and 5.8 GHz) and WiMAX bands (3.5 GHz and 5.5 GHz). The dimension of the structure is 14.50 X 27.25 mm^2 covering an area of only 395.125 mm^2. The realized antenna gain at the frequencies of interest are 2.5 dBi, 3.5 dBi, 3.5 dBi and 3.6 dBi at 3.5 GHz, 5.2 GHz, 5.5 GHz and 5.8 GHz respectively.

II. ANTENNA DESIGN

The objective of this work is to design a low-profile antenna, compact is shape and size with standard gain limits for wideband operations. The dimension of the proposed structure is 14.50 X 27.25 mm^2 covering an area of only 395.125 mm^2. Repeated square fractal geometry has been applied in design of the patch structure. The width of the feed line has been chosen to match 50 Ω impedance using (1) and (2).

For the proposed design, substrate dielectric constant, $\varepsilon_r = 4.3$, substrate height, $h = 1.5$ mm and width of feed line, $Fw = 3.0$ mm:

$$\varepsilon_{eff} = \frac{\varepsilon r+1}{2} + \frac{\varepsilon r-1}{2} \frac{1}{\sqrt{(1+12h/Fw)}}, \qquad (1)$$

$$Z_o = \frac{120\pi}{\sqrt{\varepsilon eff}\,[\frac{Fw}{h} + 1.393 + 0.667 ln\left(\frac{Fw}{h} + 1.444\right)]}, \qquad (2)$$

where Zo is the characteristic impedance and ε_{eff} is the effective dielectric constant of Substrate.

FR-4 substrate, which is commonly available in the market is used as the substrate for the proposed design.

The thickness of the substrate is kept equal to 1.5 mm. The patch and the ground plane are built of 0.5 mm thick copper plates. The patch and the ground plane is composed of Copper (annealed). The ground plane is not continuous throughout the design. A portion of the ground plane has been etched from the top. Two L-shaped slots have been introduced in the ground plane along with an I-shaped slot in the middle. The dimension of these slots have been chosen after parametric optimization. This type of etched ground structure is known as Defected Ground Structure (DGS) in antenna engineering and research. Incorporation of DGS in antenna design has an effect on frequency response of the antenna, which has been discussed later. Repeated square structures have been used in design of the patch as shown in Fig. 1.

The proposed repeated square fractal carpet geometry used to design the patch structure (Fig. 1.). The proposed antenna has been shown in Fig. 2.
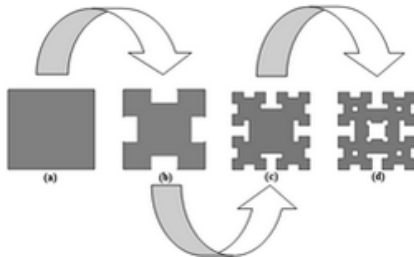
Fig. 1. Proposed fractal carpet geometry: (a) basic geometry, (b) 1st iteration, (c) 2nd iteration, and (d) 3rd iteration.
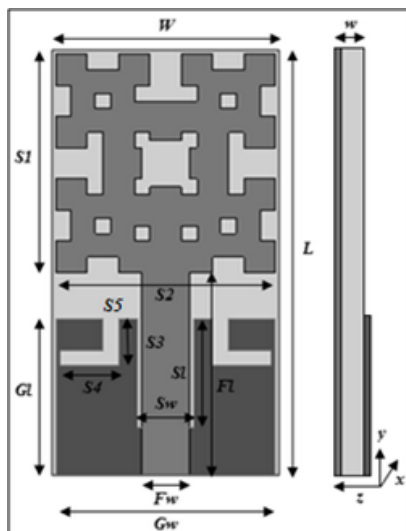
Fig. 2. Proposed fractal antenna with side view.

Genetic Algorithm (GA) has been applied for parametric optimization. The detailed parameter dimensions are provided in Table 1. It may be noted

that, the overall area of proposed structure is only $W \times L = 14.50 \times 27.25 = 395.125$ mm^2.

Table 1: Parameter dimensions (in mm)

Parameter	Dimension	Parameter	Dimension
W	14.50	Fw	03.00
L	27.25	Fl	13.00
S1	14.00	Gw	14.00
S2	14.00	Gl	10.00
S3	03.00	Sw	03.50
S4	03.75	Sl	07.00
S5	01.00	w	02.50

III. RESULTS AND DISCUSSION

The proposed antenna structure with different patch shapes in successive iterative stages has been simulated and the results have been displayed in Fig. 3.
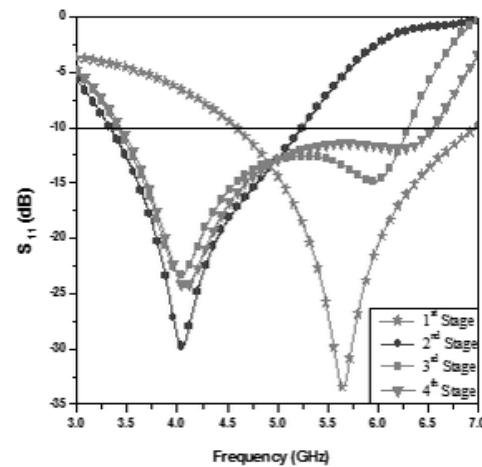
Fig. 3. Return loss of antenna at various iterative stages.

From Fig. 3, it has been observed that the resonant frequency near 5.6 GHz in the 1st stage gradually shifts towards the left near 4.0 GHz in the 2nd iterative stage with gradual interment in bandwidth in the successive stages. A maximum bandwidth of 3.13 GHz (3.42 GHz to 6.55 GHz) has been obtained, which covers the IEEE 802.11 WLAN bands (5.2 GHz and 5.8 GHz) and WiMAX bands (3.5 GHz and 5.5 GHz) in the 4th or final iterative stage.

Defected Ground Structures (DGS) are used now-a-days by antenna researchers to improve the frequency response characteristics of the antenna. A fraction of the propagating energy is stored by the ground plane, which has an effect on overall frequency response of the antenna structure. Figure 4 shows the S$_{11}$ vs. frequency plot for the antenna with and without the presence of DGS.

The proposed structure has been fabricated as shown in Fig. 5. The front view (Fig. 5 (a)) shows the fractal square patch and the 50 Ω feed line. The rear view (Fig.

5 (b)) shows the DGS ground plane. The dimension of the structure is comparable to a "1 Rupee Indian Coin". The dimension of the structure is 14.50 X 27.25 mm² covering an area of only 395.125 mm². Due to its low-profile structure, the proposed antenna has a very small coverage area and can easily be integrated in compact and low-profile devices supporting wideband operations.

frequencies of interest are 2.5 dBi, 3.5 dBi, 3.5 dBi and 3.6 dBi at 3.5 GHz, 5.2 GHz, 5.5 GHz and 5.8 GHz respectively; which is quite decent for wideband operation. Figure 9 shows the antenna surface current distribution pattern. It can be observed from that, the current originates from the feed and distributes itself uniformly at the edges of the patch. The resonant modes thereby generated, come closer resulting in a wider bandwidth.

Fig. 4. Return loss of antenna with and without DGS.
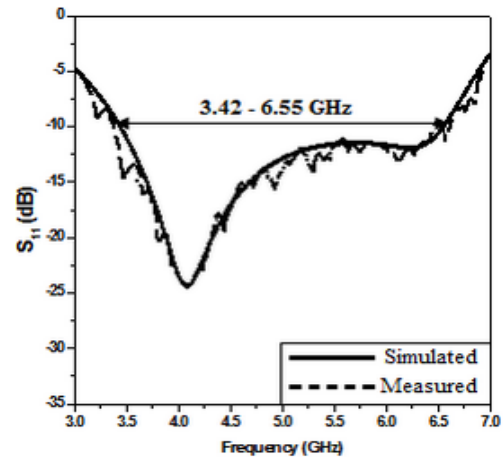
Fig. 6. Simulated and measured return losses.

Fig. 5. Fabricated prototype: (a) front view and (b) rear view.

Simulated and measured return losses have been shown in Fig. 6. The results bear a good agreement. Slight discrepancy in result may be due to the effect of soldering. 2D polar plot of the antenna has been shown in Fig. 7. Isolation level between co and cross-polarizations greater than 100 dB has been maintained with almost omni-directional H-plane patterns (Fig. 7.). The simulated and measured antenna gains are plotted in Fig. 8. The realized antenna gain (measured) at the

Fig. 7. 2D polar plot of E-plane (left) and H-plane (right) at: (a) 3.5 GHz, (b) 5.2 GHz, (c) 5.5 GHz, and (d) 5.8 GHz.
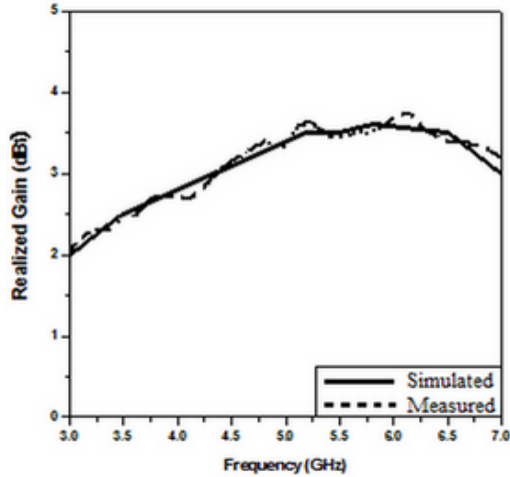
Fig. 8. Realized gain of proposed antenna.
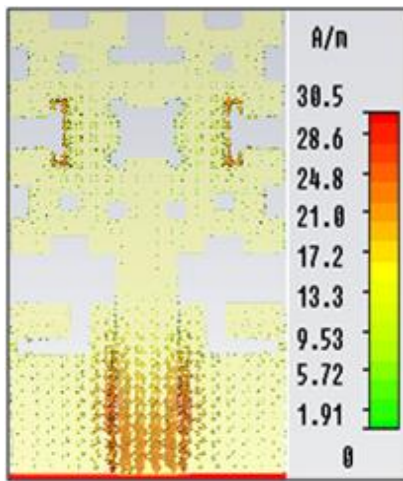
Fig. 9. Antenna surface current distribution pattern.

IV. CONCLUSION

A compact fractal monopole antenna with defected ground structure has been investigated in this paper. A wide bandwidth of 3.13 GHz (3.42 GHz to 6.55 GHz) has been obtained, which covers the IEEE 802.11 WLAN bands (5.2 GHz and 5.8 GHz) and WiMAX bands (3.5 GHz and 5.5 GHz). The dimension of the structure is 14.50 X 27.25 mm^2 covering an area of only 395.125 mm^2, which is smaller compared to other compact wideband antennas available in existing literatures. The compactness of the proposed structure with standard gain levels makes the antenna a suitable candidate for wideband communication purpose.

REFERENCES

[1] J. Gemio, J. P. Granados, and J. S. Castany, "Dual band antenna with fractal based ground plane For WLAN applications," *IEEE Antennas and Wireless Propagation Letters*, vol. 8, pp. 748-751, 2009.

[2] R. Ghatak, R. K. Mishra, and D. R. Poddar, "Perturbed Sierpinski carpet antenna with CPW feed for IEEE 802.11 A/B WLAN application," *IEEE Antennas and Wireless Propagation Letters*, vol. 7, pp. 742-744, 2008.

[3] W. Chen, G. Wang, and C. Zhang, "Bandwidth enhancement of a microstrip-line-fed printed wide-slot antenna with a fractal-shaped slot," *IEEE Transactions on Antennas and Propagation*, vol. 57, no. 7, pp. 2176-2179, 2009.

[4] K. C. Hwang, "Broad band circularly-polarised Spidron fractal slot antenna," *Electronics Letters*, vol. 45, no. 1, pp. 3-4, January 1, 2009.

[5] Y. K. Choukiker and S. K. Behera, "Design of wideband fractal antenna with combination of fractal geometries," *International Conference on Information, Communications and Signal Processing*, pp. 1-3, 2011.

[6] B. Roy, A. Bhattacharya, S. K. Chowdhury, and A. K. Bhattacharjee, "Wideband snowflake slot antenna using Koch iteration technique for wireless and C-band applications," *AEU - International Journal of Electronics and Communications*, *Elsevier*, vol. 70, iss. 10, pp. 1467-1472, 2016.

[7] S. Rosaline and S. Raghavan, "Metamaterial-inspired split ring monopole antenna for WLAN applications," *ACES Express Journal*, vol. 1, no. 5, pp. 153-156, May 2016.

Capacitance Extraction for Microstrip Lines Using Conformal Technique Based on Finite-Difference Method

Yaxiu Sun and Xiaomeng Wang

College of Information and Communication Engineering
Harbin Engineering University, Harbin, 150001, China
sunyaxiu@hrbeu.edu.cn, wangxiaomeng@hrbeu.edu.cn

Abstract — In this paper, a novel method using conformal technique of finite-difference method (FDM) is proposed to capacitance extraction of microstrip lines. Instead of deriving the average dielectric constant ε, this method uses electric field numerical weights to process the inhomogeneous cells, and takes the discontinuous effects of both inhomogeneous Ampere cell and Faraday cell into account. Besides, a new boundary condition is proposed, where the cells obeying exponential distribution are added at boundary. The new method shows good agreement with the measurement and traditional methods.

Index Terms — Capacitance extraction, conformal technique, finite-difference method (FDM).

I. INTRODUCTION

Finte-difference method (FDM) has been widely used to solve variable electromagnetic problems, especially the extraction of distributed parameters [1-3]. When solving the capacitance parameter of microstrip lines, the cells divided from the electromagnetic space can be inhomogeneous, and the dielectric constants in one cell are not unique. Thus, the difference equations cannot be used directly. The general methods solving this problem are equivalent dielectric constant techniques [4-5]. They derive the average dielectric constants according to the relationships of cell loop's volume, area and length, but have neglected the inhomogeneous Faraday and Ampere cells. So a new conformal technique is proposed in this paper, which uses the electric field numerical weights to process inhomogeneous cells, and takes discontinuous effects of Ampere and Faraday cells into account.

Besides, when FDM is used to solve the open structures, boundary conditions are required to terminate the calculation space. Generally, there are two kinds of boundary conditions. One is absorbing boundary condition (ABC) according to the traveling wave equation [6], [7]. The other is perfectly matched layer (PML) based on the absorbing media [8]. ABC requires much less computation and memory than PML, but it may cause higher reflection and larger error. Hence,

a new boundary condition is proposed, which cells obeying exponential distribution are added at the boundary. Finally, the proposed conformal technique and new boundary condition are verified by calculation.

II. FORMULATION

A. The iteration equation of FDM

The Gauss law can be represented as:

$$q = \oiint_s \boldsymbol{D} \cdot d\boldsymbol{s} , \tag{1}$$

where q is the total electric charge on the surface of the conductor, and $\boldsymbol{D}$ is the electric displacement vector which can be represented as $\boldsymbol{D} = \varepsilon \boldsymbol{E}$. Electric field intensity $\boldsymbol{E}$ can be represented by potential Φ as $\boldsymbol{E} = -\nabla\Phi$. The capacitance solving model is a dual regional structure whose dielectric constants are ε_1 and ε_2. So the spatial difference equations of $\boldsymbol{E} = -\nabla\Phi$ in these two regions can be described:

$$E_x[(i+\frac{1}{2})\Delta x, j\Delta y] = -\frac{\Phi[(i+1)\Delta x, j\Delta y] - \Phi(i\Delta x, j\Delta y)}{\Delta x}, \tag{2}$$

$$E_y[i\Delta x, (j+\frac{1}{2})\Delta y] = -\frac{\Phi[i\Delta x, (j+1)\Delta y] - \Phi(i\Delta x, j\Delta y)}{\Delta y}, \tag{3}$$

where i and j are any positive integers, Δx and Δy are the step size in x and y direction. So the divergence of electric displacement vector can be derived as:

$$\nabla \cdot \boldsymbol{D}(i\Delta x, j\Delta y)$$
$$= -\varepsilon_1 \frac{\Phi[(i+1)\Delta x, j\Delta y] + \Phi[(i-1)\Delta x, j\Delta y] - 2\Phi(i\Delta x, j\Delta y)}{(\Delta x)^2} .$$
$$- \varepsilon_2 \frac{\Phi[i\Delta x, (j-1)\Delta y] - 2\Phi[i\Delta x, j\Delta y] + \Phi[i\Delta x, (j+1)\Delta y]}{(\Delta y)^2} \tag{4}$$

If $\varepsilon_1 = \varepsilon_2$ and $\Delta x = \Delta y$, according to Laplace equation: $\nabla \cdot \boldsymbol{D} = 0$, (4) can be simplified as follows:

$$\Phi(i\Delta x, j\Delta y) = \frac{1}{4}\{\Phi[i\Delta x, (j+1)\Delta y] + \Phi[i\Delta x, (j-1)\Delta y] + \Phi[(i+1)\Delta x, j\Delta y] + \Phi[(i-1)\Delta x, j\Delta y]\} \tag{5}$$

Equation (1) can be finally updated as:

$$q = -\varepsilon \sum_{i=1}^{\infty}\sum_{j=1}^{\infty} \Phi(i\Delta x, j\Delta y) . \tag{6}$$

Equation (6) is the finite difference iteration equation to solve the capacitance, and the value of per unit length capacitance can be obtained from $C = q/V$.

B. The conformal technology based on FDM

Figure 1 shows the microstrip line model we analysis in this paper. Figure 1 (a) is the discrete grid model. Figure 1 (b) show the structure of microstrip line in Fig. 1 (a). All the simulation calculations in this paper are conducted on the basis of the model of Fig. 1 (b). As shown in Fig. 1 (a), each grid represents a cell. We can see that the dielectric constants of cells at the boundary between two regions cannot be unique. When using the new conformal technology to solve the inhomogeneous cells here, the process is divided into two parts: Faraday cell and Ampere cell.
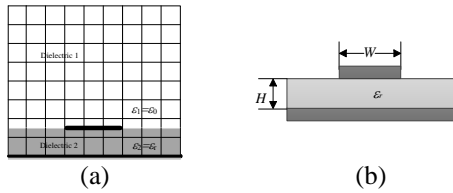

(a)   (b)

Fig. 1. (a) The discrete grid model of microstrip line, and (b) structure of microstrip line with $W/H=3$, $\varepsilon_r = 4.4$.

As shown in Fig. 2, Faraday cell is divided into two regions with different dielectric constants ε_1 and ε_2. Δx is divided into two parts: Δx_1 and Δx_2. The electric field strengths of x and y direction are also divided into two parts: E_{x1} and E_{x2}, E_{y1} and E_{y2}. θ is the angle between x direction and interface.

The spatial derivative of Faraday's law can be written as:

$$E_x^n(i+\frac{1}{2},j)\Delta x - E_x^n(i+\frac{1}{2},j+1)\Delta x + E_y^n(i,j+\frac{1}{2})\Delta y - E_y^n(i+1,j+\frac{1}{2})\Delta y$$
$$= \mu\frac{1}{\Delta t}[H_z^{n+\frac{1}{2}}(i+\frac{1}{2},j+1) - H_z^{n+\frac{1}{2}}(i+\frac{1}{2},j+\frac{1}{2})]\Delta x\Delta y$$
$$(7)$$

According to electric field boundary conditions in perfect dielectric, the weights of dielectric 1 and dielectric 2 are defined as 1 and $\varepsilon_1/\varepsilon_2$ respectively. As shown in Fig. 3, E_{x1} and E_{x2} are discontinuous. Then electric field components can be weighted and the relationship after removing weights are:

$$\begin{cases} E_{x2} = E_{2N}e_n + E_{2T}e_t \\ E'_{2N} = \varepsilon_2 E_{2N}/\varepsilon_1 \\ E'_{2T} = E_{2T} \\ E'_{x2} = E'_{2N}e_n + E'_{2T}e_t \end{cases}, \quad (8)$$

where E'_{x2}, E'_{2N} and E'_{2T} are the weighted components. e_n and e_t are unit vectors.

To ensure the integration value unchanged, the weights of electric field components are taken into integral paths and the final update relationships are:

$$\begin{cases} \Delta N_2 = \Delta x_2 \sin\theta \\ \Delta T_2 = \Delta x_2 \cos\theta \\ \dfrac{\Delta N'_2}{\Delta N_2} = (\dfrac{E'_{2N}}{E_{2N}})^{-1} = \dfrac{\varepsilon_1}{\varepsilon_2}, \\ \dfrac{\Delta T'_2}{\Delta T_2} = (\dfrac{E'_{2T}}{E_{2T}})^{-1} \\ \Delta x'_2 = \sqrt{\Delta T'^2_2 + \Delta N'^2_2} \end{cases} \quad (9)$$

where ΔN_2 and ΔT_2 are the normal component and tangential component after orthogonal decomposition of Δx_2, $\Delta N'_2$ and $\Delta T'_2$ are the component values of ΔN_2 and ΔT_2 after expanding or reducing. $\Delta x'_2$ is the total length after adjusting the path of field component. So the modified total length of the integral path can be obtained from (9):

$$\Delta x' = \Delta x_1 + \Delta x'_2 = \Delta x_1 + \Delta x_2\sqrt{\cos^2\theta + \sin^2(\theta\frac{\varepsilon_1^2}{\varepsilon_2^2})}. \quad (10)$$

So we use $\Delta x'$ instead of Δx to calculate (7).
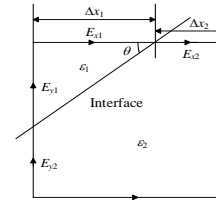
Fig. 2. The inhomogeneous Faraday cell model.
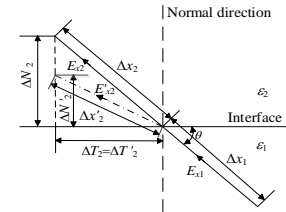
Fig. 3. The conformal process for Faraday loop path.

The conformal process of Ampere cell is same to the Faraday cell, and the Ampere cell model is shown in Fig. 4. The spatial derivative of Ampere's law can be written as:

$$H_z^{n-\frac{1}{2}}(i+\frac{1}{2},j+\frac{1}{2}) - H_z^{n-\frac{1}{2}}(i+\frac{1}{2},j-\frac{1}{2}) = \Delta y(\frac{\partial D_x}{\partial t})^n_{(i+1/2,j)}, \quad (11)$$

Δy is the total length of Ampere loop integral path.

According to electric displacement vectors boundary conditions in perfect dielectric, the weights of two kinds of media can be defined as 1 and $\varepsilon_2/\varepsilon_1$. The positional relationships are shown in Fig. 5. So the relationship between the components after removing the weights can be written as:

$$\begin{cases} D'_{2N} = D_{2N} \\ D'_{2T} = D_{2T}\,\varepsilon_1/\varepsilon_2 \end{cases}, \quad (12)$$

where D'_{2N} and D'_{2T} are the weighted components. Then taking the weights into the integral path:

$$\begin{cases} \Delta T_2 = \Delta y_2 \cos\varphi \\ \Delta N_2 = \Delta y_2 \sin\varphi \\ \dfrac{\Delta N'_2}{\Delta N_2} = \left(\dfrac{D'_{2T}}{D_{2T}}\right)^{-1} = \dfrac{\varepsilon_2}{\varepsilon_1} \\ \dfrac{\Delta T'_2}{\Delta T_2} = \left(\dfrac{D'_{2N}}{D_{2N}}\right)^{-1} \\ \Delta y'_2 = \sqrt{\Delta N'^2_2 + \Delta T'^2_2} \end{cases}, \quad (13)$$

where ΔN_2 and ΔT_2 are the initial length of normal and tangential component, which are obtained from orthogonal decomposition Δy_2, $\Delta y'_2$. $\Delta N'_2$ and $\Delta T'_2$ are the length after adjusting the path of field component. So the modified total length of the integral path is:

$$\Delta y' = \Delta y_1 + \Delta y'_2 = \Delta y_1 + \Delta y_2 \sqrt{\cos^2\phi + \sin^2\phi \frac{\varepsilon_1^2}{\varepsilon_2^2}}. \quad (14)$$

So we use $\Delta y'$ instead of Δy to calculate (11).
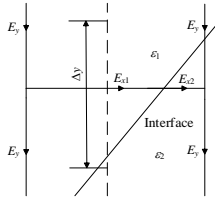
Fig. 4. The inhomogeneous Ampere cell model.
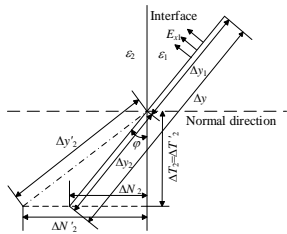
Fig. 5. The conformal process for Ampere loop path.

After above process, ε_2 and ε_1 has been converted as ε_e. So the relationship between electric field strength and electric displacement can be expressed by $\boldsymbol{D} = \varepsilon_e \boldsymbol{E}$.

C. A new boundary condition

A new boundary condition is proposed in the paper, which cells obeying exponential distribution are added at the boundary. Taking x direction for example, the electric field distribution obeys e^{-kx}, where k is a positive number. The outermost cells are considered infinitely long. When x tends to infinity, e^{-kx} is close to zero. So the outermost cells are described and the potentials are zero at infinity points.

III. NUMERICAL RESULTS

To verify the validity of new boundary condition, we use the mesh $\Delta x = \Delta y = 10^{-3}$m to calculate the region where the coordinate is $x \in [-39\Delta x, 39\Delta y]$ and $y \in [-39\Delta x, 39\Delta y]$. The potential at infinity is set at 0. We add the conductors with +10V at (-20Δx, -20Δy) and -10V at (20Δx, 20Δy) respectively.

Now the electric field distributions using different boundary conditions are shown in Fig. 6 and Fig. 7. One is the traditional boundary condition which is similar to a rectangle shield and the potential is $\Phi = 0$. The other is the new boundary condition in this paper. The electric field strength shown in Fig. 6 attenuates slowly in the diagonal direction. Whereas the electric field strength shown in Fig. 7 is closer to the potential distribution model with the same amount unlike charges. So the new boundary condition proposed in this paper is more applicable to solve the capacitance.
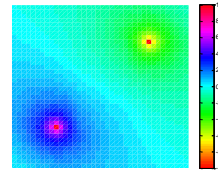
Fig. 6. The electric field distribution under traditional boundary condition.
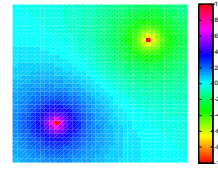
Fig. 7. The electric field distribution under new boundary condition.

Now the new method using conformal technique and new boundary condition has been applied to calculate the capacitance of microstrip line in Fig. 1. There are 79×79 grids in simulation area, and we use the mesh $\Delta x = \Delta y = 10^{-3}$m to calculate the region where the coordinate is $x \in [-39\Delta x, 39\Delta y]$ and $y \in [-39\Delta x, 39\Delta y]$. The potential at infinity is set at 0. The potential of microstrip line at [-39$\Delta x \leq x \leq$ 39Δx, -39$\Delta y \leq y \leq$ -38Δy] is +10V, and the potential of microstrip line at [-6$\Delta x \leq x \leq$ 6Δx, -35$\Delta y \leq y \leq$ -34Δy] is -10V. The dielectric constant is ε_r=4.4, which is distributed in the area of [-39$\Delta x \leq x \leq$ 39Δx, -38$\Delta y \leq y \leq$ -35Δy].

Figure 8 and Fig. 9 show the potential distributions of Fig. 1 under the new boundary. Whereas the Fig. 9 has used the conformal technique and Fig. 8 has not. The scattered field at the cross media shown in Fig. 9 is more obvious than in Fig. 8. Moreover, the per unit length capacitance obtained from Fig. 8 is 101.47pF/m, and the

value obtained from Fig. 9 is 97.759pF/m. Furthermore, the per unit length capacitance has been measured by the static field capacitance measurement method. It uses galvanometer measured the charge of microstip line in case of a given voltage. Then the per unit length capacitance can be obtained and the value is 97.761pF/m. So the value of capacitance is closer to the measurement when using new conformal technology.
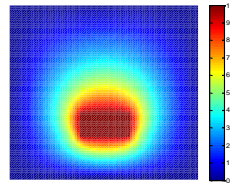
Fig. 8. The potential distribution without using conformal technique.
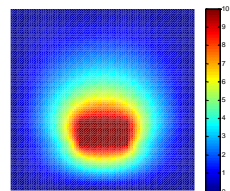
Fig. 9. The potential distribution using conformal technology.

Besides, to verify the accuracy of new method further, the average dielectric constant method has been used to calculate the capacitance of the microstip line model in Fig. 1 (b), and the discrete grid model is shown in Fig. 10. The potential distribution using the average dielectric constant method is shown in Fig. 11, and the per unit length capacitance is 96.87pF/m. The comparative result shows that the capacitance calculated by the new method is more approximated to the measurement than the average dielectric constant method. It shows that the new method has higher precision than the average dielectric constant method.

Fig. 10. The microstrip line model using average dielectric constant method.
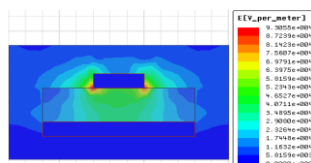
Fig. 11. The potential distribution of Fig. 10 model.

IV. CONCLUSION

A new method based on FDM has been proposed for capacitance extraction of microstrip line using conformal technique. The results show that the capacitance solved by the proposed method is close to the measurement and more accurate than traditional one. Besides, the new method can be applied to various positional relationships between dielectric interface and electric field directions. It also has a significance to the analysis and design of high speed PCB.

ACKNOWLEDGMENT

REFERENCES

[1] Y. Liu, K. Lan, and K. Mei, "Capacitance extraction for electro static multiconductor problems by on-surface MEI," *IEEE Trans. Advanc. Packag.*, vol. 23, no. 3, pp. 489-494, 2000.

[2] J. Wang, W. Y. Yin, and Q. H, Liu, "FDTD (2, 4)-compatible conformal technique for treatment of dielectric surfaces," *Electronics Lett.*, vol. 45, no. 3, pp. 146-147, Jan. 29, 2009.

[3] J. Wang, W. Y. Yin, and Y. S. Xia, "A novel conformal surface current technique for large problems based on high-performance parallel FDTD method," *IEEE Antennas and Wireless Propag. Lett.*, vol. 12, pp. 11-14, 2013.

[4] L. Liou, Y. Mah, and A. Ferendeci, "Equivalent circuit parameter extraction of microstrip coupling lines using FDTD method," *IEEE Int. Symp. Antennas Propag.*, vol. 3, pp. 2488-1491, 2000.

[5] W. Yu and R. Mittra, "A conformal finite difference time domain technique for modeling curved dielectric surfaces," *IEEE Microw. Wireless Comp. Lett.*, vol. 11, no. 1, pp. 25-27, Jan. 2001.

[6] J. Zhou and J. Zhao, "Efficient high-order absorbing boundary conditions for the ADI-FDTD method," *IEEE Microw. Wireless Comp. Lett.*, vol. 19, no. 1, pp. 25-27, Jan. 2009.

[7] H. Shao, W. Hong, and Y. Zhou, "Generalized Z-domain absorbing boundary conditions for the analysis of electromagnetic problems with finite-difference time-domain method," *IEEE Trans. Microw. Theory Tech.*, vol. 51, pp. 82-90, 2003.

[8] S. Wang and F. L. Teixeira, "An efficient PML implementation for the ADI-FDTD method," *IEEE Mirow. Wireless Compon. Lett.*, vol. 13, no. 2, pp. 72-74, Feb. 2003.

Ultra-Wideband Microstrip Antenna for Body Centric Communications

Amin Darvazehban [1] and Taraneh Rezaee [2]

[1] Department of Computer and Electrical Engineering
Amirkabir University of Technology, Tehran, Iran
Amin.darvazehban@gmail.com

[2] Department of Biomedical Engineering
Islamic Azad University, Tehran, Iran
Taraneh.rezaii@yahoo.com

Abstract ─ A novel low profile reconfigurable wide band microstrip antenna for impulse radio ultra-wideband (IR-UWB) WBANs and targeted for on-body sensor node has been introduced. The printed monopole antenna consists of a heart shaped radiating patch and an elliptical ground plane. This antenna has a frequency bandwidth of 130% with a VSWR of 1.5 and average gain is about 3.6 dBi. There is a slot on the patch which is loaded by two varactor diodes to form a tunable notch band. The antenna operates from 2.4 GHz to 12 GHz. The proposed antenna is a good candidate for medical purpose since it has a sufficient amount of gain and bandwidth. We used active circuit to increase the flexibility of setting rejection band to prevent having interference from other sources such as Wi-Fi. The antenna is fabricated and there is a good agreement between the simulation and measurement results.

Index Terms ─ Body-centric wireless communication, miniaturized microstrip antenna, wireless body networks.

I. INTRODUCTION

Antenna designing for WBAN system is challenging due to the human body effect. Especially, providing the sufficient gain and efficiency of an antenna is the main issue of on-body to on-body communication. To overcome this problem, an on-body antenna should have vertical polarization relative to the human body surface. In addition, to satisfy the propagation along the body surface for on-body to on-body communication, the antenna is required to have omnidirectional radiation characteristic [1]. Also, a number of techniques aimed at minimizing the cost of such antenna without significantly sacrificing performance have been considered. One of the most important techniques is using slots on the patch surface. Slots perturb antenna current on the antenna surface and increase antenna bandwidth [2]. Another advantage of using slots is changing antenna polarization or using as a Frequency Selective Surface (FSS) to filter

unwanted frequencies [3]. In some paper, small slots are imbedded on ground plane or feeding point to have better matching response. These techniques are well-known as Defected Ground Structure (DGS) and Defected Microstrip Structure (DMS) [4]. PIN diodes have been also used to change the antenna dimensions electrically and increase the frequency bandwidth [5]. In this paper, we use varactor diodes to increase the frequency bandwidth. The varactor diode is a variable capacitor which can be modelled as a series capacitor and a resistor to model the ohmic losses [6, 7]. To improve frequency and pattern bandwidth, heart-shaped printed monopole antenna is proposed in [8]. In this paper, a low profile ultra-wideband on-body antenna is presented. The proposed antenna has a low profile, omnidirectional radiation patterns in the whole UWB band, and maximum radiation along the near body surface. We also use antenna with slot and taper heart-shaped to increase frequency bandwidth. In some purposes we need filter to cut the frequency bandwidth, two varactor diodes are used to change the notch in frequency bandwidth. When we change the DC bias of the diodes, their capacitance values change. So this antenna is combination of filter and antenna. The proposed low profile UWB antenna is suitable for on-body communications since the field is vertically polarized and propagated along the body surface for IEEE 802.11b/g and IEEE 802.11a. The antenna is considered to operate as a relay between sensors located on the body and non-local station so it is an advantage for the antenna to be able to have tangential radiation over the body surface in the on-body mode and a bore sight pattern in the off-body mode at the frequency bands of 802.11a and 802.11b/g, respectively [9, 10]. This antenna has a frequency bandwidth of 130% with a VSWR of 1.5, average gain is about 3.6 dBi.

II. DESIGN OF A SLOTTED MICROSTRIP ANTENNA

As it is shown in Fig. 1, the proposed slot antenna

with line feed has been designed on Rogers RO4003 with permittivity of ε_r=3.2 and substrate thickness of h=0.813 mm and substrate size of 42×30 mm. The dimensions of slots and antenna are mentioned in Table 1.
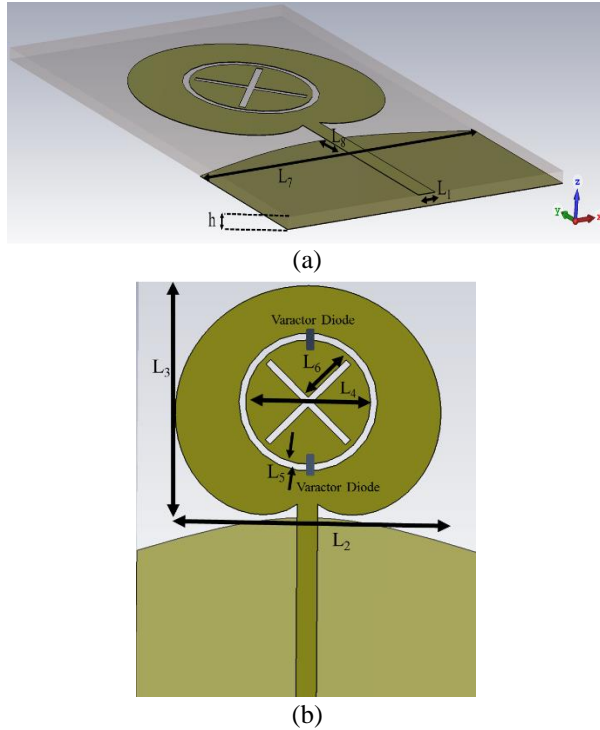

(a)

(b)

Fig. 1. Proposed slotted microstrip antenna: (a) side view, and (b) top view.

Table 1: Physical dimension of loaded-monopole

Parameter	L_1	L_2	L_3	L_4	L_5
Dimension (mm)	1.8	22	20	10	0.5
Parameter	L_6	L_7	L_8	h	
Dimension (mm)	4.7	30	2.3	0.813	

Two varactor diodes are used to change the capacitance value of the circular slots and these slots create notch in the frequency band. The notch band avoid interference with other frequency bands. Circular slots create notch in the frequency band. Line feed should be adjusted for 50Ω transmission line [11].

To increase the frequency bandwidth, two crossed slots are designed on the surface of the microstrip patch. These slots decrease antenna patch area and based on the following formula, quality factor of the microstrip antenna decreases. S is the area of the patch and f_r is the resonant frequency of the microstrip antenna. Frequency shift for patch is given as [12]:

$$\left| \frac{\Delta S}{S} \right| = \frac{1}{Q_0} , \qquad (1)$$

$$\Delta f_1 = f_{0r} / 2Q_0 . \qquad (2)$$

III. RESULTS AND DISCUSSION

With the dimensions given in Table 1, the proposed antenna was simulated in close proximity of the human body. To obtain the human effect on the antenna behavior, VOXEL model of body with CST software is simulated. The human body model was developed in the CST microwave studio. It is an adult male of mass 100 kg, height 180 cm and chest circumference of 115 cm, including muscle, skeleton and brain with human tissue. The electrical properties were defined at the frequency band of 2.5-12 GHz with resolution of 100 MHz. Figure 2 shows the placement of the antennas on the model. The antenna is placed 2 mm apart from the chest of the model. The on body simulated and measured S_{11} of the proposed antenna are illustrated in Fig. 3 and Fig. 5. As shown in Fig. 3, the bandwidth of the antenna can be changed from 2.5 GHz to 12 GHz in transmitting purposes and 2 GHz to 12 GHz in receiving purposes. As it is shown in Fig. 6, the human body behaves like a reflector and improves gain of the antenna because the permittivity of the body is about 42. The backlobe part of the antenna pattern is removed. In these types of antennas each part of the antenna has different resonant frequency, therefore the impedance bandwidth is wider than typical microstrip antenna. To obtain better results all dimensions are optimized. We have used Particle Swarm Algorithm with CST software. It is observed that the variation in the diameter of the metallic arcs has major effect on the lower frequency bandwidth. In case of impedance bandwidth, it improves return loss at higher frequency region and does not affect the lower cut-off frequency. The simulated antenna VSWR referenced to 50Ω is shown in Fig. 4. The improvement in the input impedance bandwidth using slots and curved ground plane is clear. It is interesting to mention that at low frequencies, the input impedance of the antenna is depended on the patch dimensions not the substrate dimensions.

At high frequencies the input impedance is intensively affected by the substrate thickness. We can improve matching parameter using elliptical ground plane. It is obvious that the radiation patterns changes slightly at higher frequency because of variation antenna dimensions at different frequencies. It means that radiation pattern bandwidth is smaller than impedance bandwidth. In portable system, this is negligible since we do not have constant and stable direction for transmitter. This antenna is so small and can be used in medical purposes. For example, in some frequencies such as Wi-Fi, interference is inevitable and we need an antenna that can filter unwanted frequencies. These diodes are used for creating notch to reject these frequencies. In this paper we used tapered elliptical form for the structure to get better impedance matching. The radiation patterns

of the antenna when the antenna is attached to the body are changed. The body behaves like a reflector because the body permittivity $\varepsilon_r=42$ is so high. To verify the simulation result, the antenna has been fabricated and tested (see Fig. 7).

(a) Remote view

(b) Close view
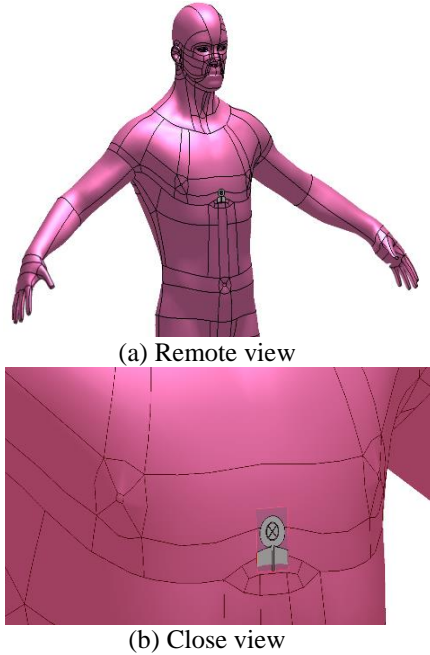
Fig. 2. The proposed antenna placed on the chest human body model.
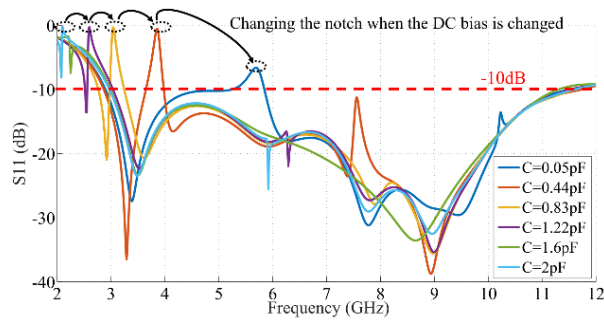
Fig. 3. Simulated S_{11} with CST software for different capacitance values on body.
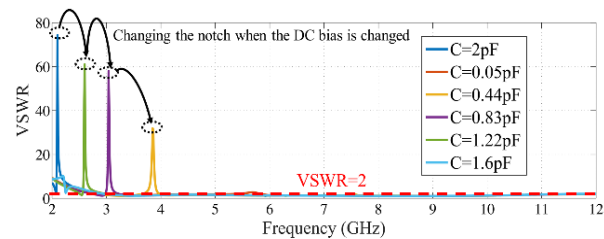
Fig. 4. VSWR of the slotted microstrip antenna.
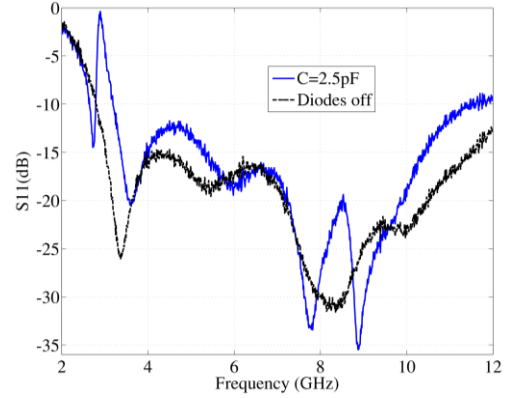
Fig. 5. Measured S_{11} in two states: 1-Diodes ON, 2-Diodes OFF.

f=2 GHz, Gain=1.28 dB   f=2 GHz, Gain=8.26 dB

f=6 GHz, Gain=3.68 dB   f=6 GHz, Gain=8.98 dB

f=12 GHz,Gain=4.58 dB   f=12 GHz, Gain=9.3 dB

Fig. 6. Comparision of the antenna radiation patterns at different frequencies with human body and without human body.
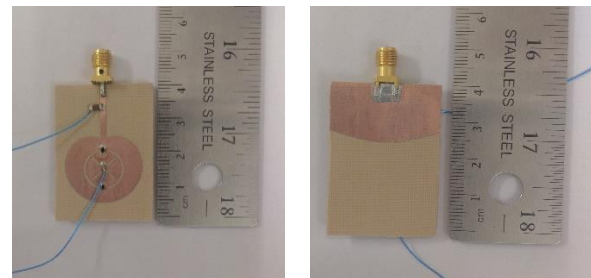
Fig. 7. Photo of fabrication.

VI. CONCLUSION

An efficient wide band and dual pattern heart-patch antenna with two varactor diodes and strip line feed is proposed for on-body and off-body communication modes is proposed and analysed with respect to the bandwidth, average gain, radiation pattern. The impedance bandwidth of proposed antenna achieved 130% from frequency range 2.8 to 12 GHz. The average gain of the antenna is about 3.5 dBi. The radiation pattern of E- plane & also studied. It has Bi-directional E-plane & Omni-directional H-plane. This antenna is simple in structure and easy to fabricate with MIC/MMIC systems. This antenna can be used for wireless communication systems, especially for medical purposes. We can adjust notch frequency band of the antenna easily by changing DC bias of the varactor diodes. The proposed antenna presents much improved gain with one tapered shape radiating element than the previous works of the compact dual band and dual mode antennas. The results show that this antenna does not experience significant frequency detuning from the free space resonance at whole frequency bands when simulated on the human body.

REFERENCES

[1] G. A. Conway and W. G. Scanlon, "Antennas for over body-surface communication at 2.45 GHz," in *Antennas and Propagation, IEEE Transactions on*, vol. 57, no. 4, pp. 844-855, Apr. 2009.

[2] K. M. Chang, R. J. Lin, I. C. Deng, J. B. Chen, K. Q. Xiang, and C. J. Rong, "A novel design of a CPW-fed square slot antenna with broadband circular polarization," *Microwave. Opt. Technol. Lett.*, vol. 48, no. 12, pp. 2456-2459, Dec. 2006.

[3] O. Manoochehri, S. Abbasiniazare, A. Torabi, and K. Forooraghi, "A second-order BPF using a miniaturized-element frequency selective surface," *Progress In Electromagnetics Research C*, vol. 31, pp. 229-240, 2012.

[4] M. A. Salari, O. Manoochehri, and S. Abbasiniazare, "Miniaturized microstrip ring hybrid with defected microstrip structure," *Microwave and Optical Technology Letters*, vol. 55, pp. 2245-2248, 2013.

[5] S. Abbasiniazare, O. Manoochehri, and K. Forooraghi, "A reconfigurable printed dipole antenna using RF PIN diodes," *Microwave and Optical Technology Letters*, vol. 56, pp. 1151-1155, 2014.
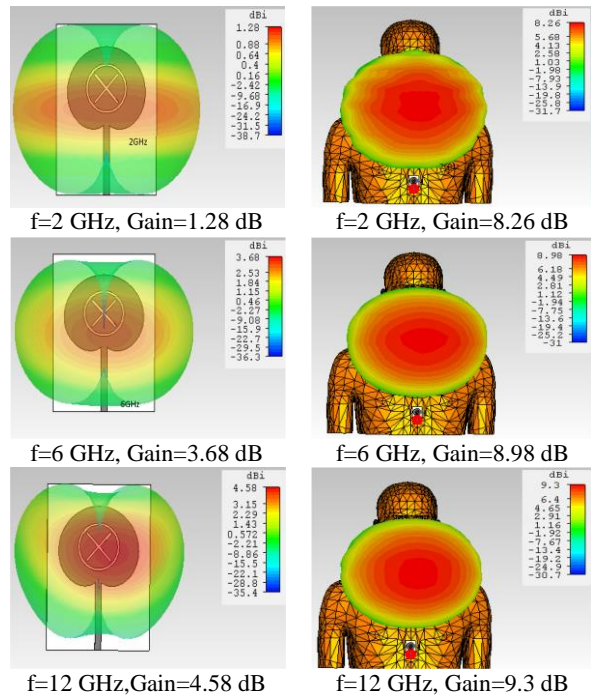
[6] M. Norooziarab, Z. Atlasbaf, M. Rafaei-Booket, and F. Farzami, "A tunable transmission line based on an SIW loaded by a new single-cell meta-material," *Telecommunications (IST), 2012 Sixth International Symposium on*, Tehran, pp. 75-79, 2012.

[7] F. Farzami and M. Norooziarab, "Experimental realization of tunable transmission lines based on single-layer SIWs loaded by embedded SRRs," in *IEEE Transactions on Microwave Theory and Techniques*, vol. 61, no. 8, pp. 2848-2857, Aug. 2013.

[8] C. Hua, Y. Lu, and T. Liu, "Printed UWB heart-shaped monopole antenna with band-notch reconfigurability," in *2016 IEEE International Workshop on Electromagnetics: Applications and Student Innovation Competition (iWEM)*, pp. 1-3, 2016.

[9] G. A. Conway, W. G. Scanlon, and D. Linton, "Low profile microstrip patch antenna for over-body surface communication at 2.45 GHz," in *Vehicular Technology Conference, 2007, VTC2007-Spring, IEEE 65th*, pp. 392-396, Apr. 22-25, 2007.

[10] S. Khaledian and Z. Atlasbaf, "Dual band and dual mode microstrip antenna for body centric wireless communication," *Applied Computational Electro-magnetics Society Journal*, vol. 31, 2016.

[11] I. J. Bahl and R. Garg, "A designer's guide to stripline circuits," *Microwaves*, pp. 90-96, Jan. 1978.

[12] J. R. James, et al., *Microstrip Antenna Theory and Design*. Steven-age, UK: Peter Peregrinus, 1981.

A Simple Analytical Method to Calculate Bending Loss in Dielectric Rectangular Waveguides

Kim Ho Yeap, Andrew Wei Chuen Tan, Koon Chun Lai, and Humaira Nisar

Faculty of Engineering and Green Technology
Tunku Abdul Rahman University, Kampar, Perak, 31900, Malaysia
yeapkh@utar.edu.my, evilfire8laster@1utar.my, laikc@utar.edu.my, humaira@utar.edu.my

***Abstract* ─** We present a simple analytical method to compute attenuation in bent dielectric rectangular waveguides. An approximate formulation for the attenuation constant is first derived by determining the ratio of average power loss per unit length to the average power propagating along the waveguide. Since the waveguide has been simplified into a slab in the process of derivation, losses at the four edges of the structure have been neglected. To account for these losses, the perturbation theory has been employed. The total loss is found to agree closely with that obtained via the Finite Element Method (FEM). Unlike the FEM which requires considerable computational time and power to solve, we demonstrate that the analytical method proposed here can easily be applied and it gives sufficiently accurate result.

***Index Terms* ─** Analytical method, attenuation constant, bending loss, perturbation theory, propagation constant, rectangular waveguides.

I. INTRODUCTION

Dielectric waveguides, such as optical fibers, have been widely used in the fields of telecommunication and integrated optics to channel signal from one end to another. In a dielectric waveguide, the core dielectric rod is immersed in one or more layers of dielectric materials which are of lower index of refraction n_2 than the core material itself n_1. This allows wave to propagate in the waveguide based on the principle of total internal reflection, described by Snell's law [1, 2]. In order to ensure that the information carried by the modulating signal is preserved, it is important to minimize losses in the waveguide during wave propagation. The losses in a dielectric waveguide can generally be classified into dielectric loss and radiation loss. In a uniformly straight waveguide, the fields are mostly confined within the core of the waveguide. Hence, radiation loss is practically negligible in the waveguide. When certain curvatures occur in the waveguide, however, wave with angles of incident exceeding the critical angle tend to radiate out from the guiding structure [3]. Because of this reason,

radiation loss or more commonly known as bending loss, in this case, can no longer be ignored. Since bent structures are inevitable when channeling the signal, both dielectric and bending losses are equally important when estimating the total loss in the waveguide. Developing mathematical expression to describe the presence of curvatures in a rectangular waveguide is inherently difficult. This is because a combination of Cartesian and cylindrical coordinates is required so as to define the cross section and the bending radius of the waveguide. Hence, analytical methods, found in most literatures [4-7], focus only on the analyses of uniformly straight waveguides. As can be seen from some of the recent literatures [8-11], computational methods such as Finite Domain Time Difference (FDTD) or Finite Element Method (FEM) are preferred when bending loss is to be accounted for in the calculation of loss. The algorithms used in computational methods discretize the solution space into meshes. The electric field in each mesh is then numerically calculated. Hence, although they produce accurate results, these methods typically consume substantial computational time and power. This is particularly true when fields are to be solved for signals with very small wavelength (such as THz or optical signal) propagating in a three dimensional structure where the number of meshes is exceptionally huge. Analytical methods, on the other hand, are simpler and require relatively less time and power to solve.

Marcatili [3] and Marcuse [12] were among some of the early researchers who had developed analytical solutions for bent rectangular waveguides. In the process of derivation, however, both of them had assumed the fields' radiation at the four corner regions of the waveguide to be negligible. Due to this reason, the loss found using their methods has been underestimated. It is worthwhile noting that, Marcatili's method is only valid when the wave is weakly guided (i.e., the difference between n_1 and n_2 is small), while Marcuse's method is not bounded by this limitation. Hence, Marcuse's method has the advantage of being applied in structures with arbitrary ratio of indices of refraction. In this paper, we present an improvement on the accuracy of

Marcuse's method. We consider a dielectric rectangular waveguide surrounded by homogeneous dielectric material in our study. In order to account for the loss at the corner regions, we incorporate into the formulation the correction factor developed by Deck et al. [13]. This paper shall be presented in such a way that, casual readers could appreciate the final mathematical expressions, without the need of going through the underlying mathematics.

II. FORMULATION

Figure 1 depicts the structure of a bent rectangular waveguide with width a and height b. When deriving the attenuation constant of the waveguide, Marcuse has first assumed the fields at the vicinity of a bent waveguide to be similar to that of a straight guide. The assumption should hold valid as long as the radius of curvature R is sufficiently large. When deriving the fields' expressions, he has also assumed that there is no field variation in the y direction. This allows the propagating waves to be described as simple TE and TM waves [12]. According to the law of conservation of energy, the rate of decrease of power is to be equivalent to the power loss. Hence, power loss Λ can be expressed as the ratio of average power loss per unit length Δp to the average power propagating along the waveguide p, i.e., [1, 12]:

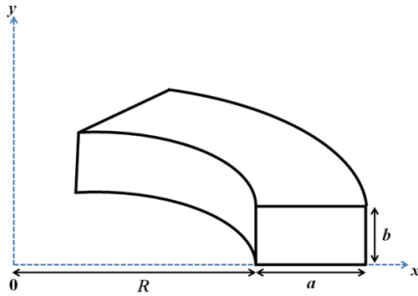$$\Lambda = \frac{\Delta p}{p}. \tag{1}$$

Fig. 1. A bent rectangular waveguide.

By substituting the fields' expression into (1), the loss equation Λ can be obtained as follows [12]:

$$\Lambda = \mathrm{Im} \left| \frac{2\sqrt{k_z^2 - n_2^2 k_2^2}\left(n_1^2 k_2^2 - k_z^2\right)}{k_2^2 k_z \left(n_1^2 - n_2^2\right)} \times \right.$$
$$\left. \frac{\exp\left[a\sqrt{k_z^2 - n_2^2 k_2^2} - \frac{2\left(k_z^2 - n_2^2 k_2^2\right)^{1.5}\left(R + 0.5a\right)}{3 k_z^2} \right]}{\left[a + \frac{1}{\sqrt{k_z^2 - n_2^2 k_2^2}} + \frac{1}{\sqrt{k_z^2 - n_1^2 k_2^2}} \right]} \right|, \tag{2}$$

where k_2 is the wavenumber of the dielectric cladding

material and k_z is the propagation constant, which can be adopted from that of a straight waveguide. It is to be noted that k_z is a complex variable which comprises a phase constant β_z and an attenuation constant α_z, i.e., $k_z = \beta_z - j\alpha_z$. Here, we have applied the closed-form expression for k_z, modified from [14] as shown below:

$$k_z = \left\{ k_1^2 - \left(\frac{m\pi}{a}\right)^2 - \left(\frac{n\pi}{b}\right)^2 + \right.$$
$$\left. 2(1-j)\frac{\delta\mu_1}{a\mu_2}\left[\left(\frac{m\pi}{a}\right)^2 + \left(\frac{n\pi}{b}\right)^2 + k_1^2\right]\right\}^{0.5}, \tag{3}$$

where k_1 is the wavenumber of the core material, μ_1 and μ_2 are respectively the permeability of the core and cladding materials; whereas m and n are respectively the number of half cycle variations in the x and y directions. The skin depth δ in (3) is given by [15]:

$$\delta = \frac{2Z_S}{(1+j)\omega\mu_2}, \tag{4}$$

where ω is the angular frequency. The surface impedance of the dielectric layer Z_S can be expressed in terms of the electrical properties of the two mediums as [7, 16]:

$$Z_S = \frac{1}{j\omega b(\varepsilon_{r1} - \varepsilon_{r2})}, \tag{5}$$

where ε_{rd} and ε_{r0} are respectively the relative permittivity of the core and the cladding materials. To account for the loss at the four corner regions, we employ the formulation developed by Deck et al. [13] by means of the perturbation theory. When deriving the correction to the mode propagation and profile function, correction to the dielectric function in the four corner regions is assumed to produce changes in the squared propagation constant and fields profile function [13]. The corner field correction factor $\Delta\Lambda$ can be expressed as [13]:

$$\Delta\Lambda = \mathrm{Im}\left| \left(\frac{\varepsilon_1 - \varepsilon_2}{2}\right)\left(\frac{\omega}{c\gamma}\right)^2 \times \right.$$
$$\left\{1 + \left[\cos(k_y b) + \left(\frac{\varepsilon_1}{\varepsilon_2}\right)\left(\frac{\gamma}{k_y}\right)\sin(k_y b)\right]^2\right\} \times$$
$$\left. \frac{(2\gamma b + 1)}{1 + \left[\cos(k_y b) + \left(\frac{\varepsilon_1}{\varepsilon_2}\right)\left(\frac{\gamma}{k_y}\right)\sin(k_y b)\right]^2} \Lambda \right|, \tag{6}$$

where ε_1 and ε_2 are respectively the permittivity of the core and its cladding material, $\gamma = \left(\frac{\omega}{c}\right)^2(\varepsilon_1 - \varepsilon_2) - k_y^2$ and k_y is the transverse wavenumber in the y direction. For simplicity, we apply the closed-form expression of k_y in [6] as shown in (7) below:

$$k_y = \frac{\pi}{b}\left(\frac{\pi n_1^2 b\sqrt{n_1^2 - n_2^2}}{\pi n_1^2 b\sqrt{n_1^2 - n_2^2} + n_2^2\lambda}\right). \tag{7}$$

The total bending loss Λ_T can therefore be determined by including the additional loss found in (6) with the loss in (2), i.e., $\Lambda_T = \Lambda + \Delta\Lambda$.

III. RESULTS AND DISCUSSION

We compute the loss in a 2.4×1.3 mm^2 silicon rectangular waveguide, with bending radius $R = 1$ mm. The conductivities of silicon and the surrounding medium are given as 4.33×10^{-4} S/m and 8.0×10^{-15} S/m, respectively. To validate the closed-form formulations presented here, we compare the computed results with the S21 parameters found from the Finite Element Method (FEM). The results from FEM are simulated from Ansoft's High Frequency Structure Simulator HFSS. Since S21 accounts for the total loss in the waveguide, we have incorporated the total dielectric loss α_z, i.e., the imaginary component of (3) together with the bending loss in (2) during comparison. When calculating the loss, we have set $m = 1$ and $n = 0$ for the dominant TE mode. It is worthwhile noting that, the loss in a practical waveguide may also be contributed from the imperfection of the waveguide structure. Since the work presented here is a theoretical exercise, such loss has therefore been neglected.

Figure 2 depicts the comparison of loss between our computed result and that obtained from HFSS. It can be seen from the figure that although the curves agree somewhat with each other, the loss from the computed result has clearly been underestimated. The average error with reference to the FEM result $\varepsilon_{ave} = 60.17\%$. Since Marcuse has neglected the presence of the electric field in the x direction E_x, the loss of the E^x mode has not been taken into account. As shown in [6], the modes propagating in a dielectric waveguide are degenerate – both E^y and E^x modes exist concurrently and that the propagation constants of both modes are similar to each other. Figure 3 shows the total loss (i.e., the addition of dielectric and bending losses) when both E^x and E^y modes are taken into account. It can be observed from Fig. 4 that the electric fields of the E^x and E^y modes are orthogonal to each other. Despite their direction of polarizations, however, the profiles exhibited by both modes are qualitatively similar to each other [3]. Here, we have taken the bending loss exhibited by the E^x mode to be identical with that by E^y. The result turns out to be in closer agreement with that obtained from the FEM method, although discrepancy between the results is still apparent ($\varepsilon_{ave} = 44.53\%$). Figure 5 shows the final result when the corner field correction factor $\Delta\Lambda$ has been included into our calculation. By considering the loss at the four edges of the waveguide, it can be observed from the figure that the result improves significantly, with

the computed result approaches that of the simulation ($\varepsilon_{ave} = 21.27\%$).

Fig. 2. Loss of a bent rectangular silicon waveguide, obtained from the analytical method proposed here (solid line) and the FEM (dashed line). The analytical method has only considered the dielectric loss and the bending loss from the E^y mode (loss at the corner regions has been neglected).

Fig. 3. Loss of a bent rectangular silicon waveguide, obtained from the analytical method proposed here (solid line) and the FEM (dashed line). The analytical method has only considered the dielectric loss and the bending loss from the E^y and E^x modes (loss at the corner regions has been neglected).

(a)   (b)

Fig. 4. Electric field lines of: (a) E^x and (b) E^y modes at the cross section of the rectangular waveguide.
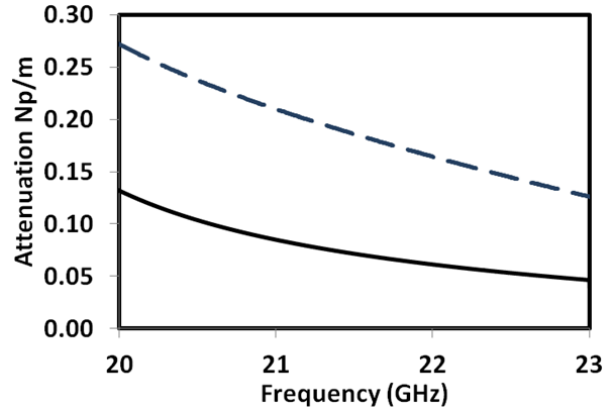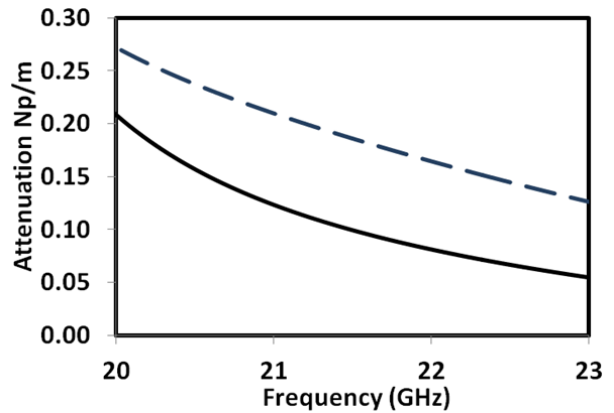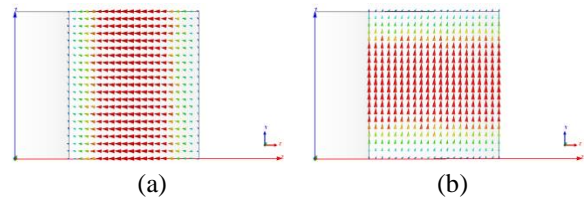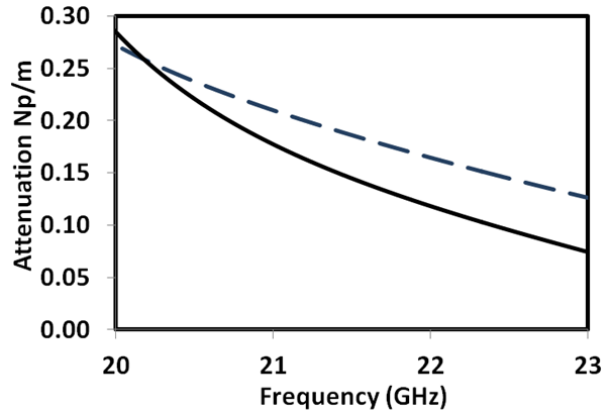
Fig. 5. Loss of a bent rectangular silicon waveguide, obtained from the analytical method proposed here (solid line) and the FEM (dashed line). The analytical method has taken into account the dielectric loss, as well as, the bending loss from the E^y and E^x modes (loss at the corner regions has been included).

IV. CONCLUSION

We have presented a closed-form analytical method to predict the attenuation in a bent dielectric rectangular waveguide. The dielectric loss in the waveguide can be extracted from the propagation constant obtained from a straight waveguide; whereas, the bending loss in the waveguide is determined from Marcuse' approximate method [12]. To enhance the accuracy of Marcuse' method, the correction factor in [13] has been applied to account for the loss at the corner regions. By including the bending loss exhibited by both E^y and E^x modes and the dielectric loss, the result is found to agree closely with that computed using the rigorous computational method. Since the formulations presented here are all in closed-form, it is not necessary to rely on computational intensive machines, such as a computer to calculate them. Besides being straight forward, the method also produces results which can be easily found; while at the same time, sufficiently accurate.

REFERENCES

[1] D. K. Cheng, *Field and Wave Electromagnetics*. 2nd ed., Addison Wesley Inc., 1989.

[2] R. E. Collin, *Field Theory of Guided Waves*. 2nd ed., IEEE Press, New York, 1991.

[3] E. A. J. Marcatili, "Bends in optical dielectric guides," *The Bell System Technical Journal*, vol. 48, no. 9, pp. 2103-2132, 1969.

[4] Y. Cai, T. Mizumoto, and Y. Naito, "Improved perturbation feedback method for the analysis of rectangular dielectric waveguides," *Journal of Lightwave Technology*, vol. 9, no. 10, pp. 1231-1237, 1991.

[5] P. R. Young and R. J. Collier, "Solution of lossy dielectric waveguides using dual effective-index method," *Electronics Letters*, vol. 33, no. 21, pp. 1788-1789, 1997.

[6] E. A. J. Marcatili, "Dielectric rectangular waveguide and directional coupler for integrated optics," *The Bell System Technical Journal*, vol. 48, no. 9, pp. 2071-2102, 1969.

[7] K. H. Yeap, K. H. Teh, K. C. Yeong, K. C. Lai, and M. C. Loh, "Propagation in dielectric rectangular waveguides," *Optica Applicata*, vol. 46, no. 2, pp. 317-330, 2016.

[8] D.-P. Cai, S.-C. Nien, H.-K. Chiu, C.-C. Chen, and C.-C. Lee, "Electrically tuneable liquid crystal waveguide attenuators," *Optics Express*, vol. 19, no. 12, pp. 11890-11896, 2011.

[9] H.-K. Chiu, F.-L. Hsiao, C.-H. Chan, and C.-C. Chen, "Compact and low-loss bent hollow waveguides with distributed Bragg reflector," *Optics Express*, vol. 16, no. 19, pp. 15069-15073, 2008.

[10] S.-S. Lo, C.-C. Chen, S.-C. Hsu, and C.-Y. Liu, "Fabricating a hollow optical waveguide for optical communication applications," *Journal of Microelectromechanical Systems*, vol. 15, no. 3, pp. 584-587, 2006.

[11] S.-S. Lo, M.-S. Wang, and C.-C. Chen, "Semiconductor hollow optical waveguides formed by omni-directional reflectors," *Optics Express*, vol. 22, no. 26, pp. 6589-6593, 2004.

[12] D. Marcuse, "Bending losses of the asymmetric slab waveguide," *The Bell System Technical Journal*, vol. 50, no. 8, pp. 2551-2563, 1971.

[13] R. T. Deck, M. Mirkov, and B. G. Bagley, "Determination of bending losses in rectangular waveguides," *Journal of Lightwave Technology*, vol. 16, no. 9, pp. 1703-1714, 1998.

[14] P. I. Somlo and J. D. Hunter, "On the TE10 mode cutoff frequency in lossy-walled rectangular waveguides," *IEEE Transactions on Instrumentation and Measurement*, vol. 45, pp. 301-304, 1996.

[15] T. K. Hong, "Analysis of Loss in Dielectric Waveguides," *Universiti Tunku Abdul Rahman*, Malaysia, B.Eng., 2014.

[16] B. M. Kolundžija and A. R. Djordjević, *Field Integral Equations*. In: Electromagnetic Modeling of Composite Metallic and Dielectric Structure, Artech House, Massachusetts, pp. 181-182, 2002.

Ultra-Wide Bandwidth Enhancement of Single-Layer Single-Feed Patch Antenna Using the Theory of Characteristic Modes

Mohamed M. Elsewe and Deb Chatterjee

Computer Science & Electrical Engineering Department
University of Missouri – Kansas City, Kansas City, MO 64110, USA
mme0f0@mail.umkc.edu, chatd@umkc.edu

Abstract ─ The Theory of Characteristic Modes (TCM) is proposed as a systematic approach to antenna design to achieve the goal of finding the antenna structure with optimum broadband behavior. This theory provides a physical insight to the radiating nature of microstrip patch antennas and reduces the design optimization time. In this work, the resonant behavior of the highly radiating structure of the single U-slot rectangular patch on a single-layer $\varepsilon_r = 4.4$ substrate is analyzed using TCM. Modal analysis of this single-layer structure with different single feed excitations concludes that VSWR ≤ 2 impedance bandwidth in the order of 96% can be achieved with a single T-probe feed. Experimental results, included here, show VSWR ≤ 2 impedance bandwidth in the order of 71%.

Index Terms ─ Bandwidth broadening, characteristic mode analysis, L-probe, microstrip patch antennas, T-probe, theory of characteristic modes, U-slot, UWB.

I. INTRODUCTION

The need for antennas with high bandwidth is continuing to fuel a lot of research especially in the fields of radar, wireless communication and medical imaging. Microstrip patch antennas are a class of antennas that exhibit low-profile, compact, conformal, cost-effective, and easy-to-fabricate designs. Despite these advantages, microstrip patch antennas suffer from a major drawback, which is narrow bandwidth. For the past couple of decades, extensive research has been dedicated to the area of bandwidth broadening techniques of microstrip patch antennas. Some of these techniques are by means of introduction of parasitic elements and patch slots, which introduce additional resonances in addition to the main patch resonance. Another technique is by means of thick substrates of low permittivity, which will have the side effect of introducing higher inductive reactance due to the longer coaxial feed probe. Some of the patch slot geometries found in the literature are: square, rectangular, triangular, circular, elliptical, E-slot, U-slot, V-slot, and more [1, 2]. Although it is generally understood that patch slots introduce new resonances that contribute to broadening the bandwidth, it is not well understood why some patch slots present better bandwidth than others. A valuable tool that is helping antenna designer's gain better understanding and physical insight of the radiating nature and resonant behavior of the microstrip patch antenna is the TCM [3, 4]. By understanding the resonant behavior of the different patch slot geometries and other antenna elements, novel antenna designs with the most resonant structures can be proposed to achieve the most radiation and impedance bandwidth.

In recent studies [5-7], we utilized TCM to characterize the resonant behavior of different patch slot geometries, substrate permittivities and ground sizes independent of the feeding element to identify the structures which are more resonant, and hence, contribute significantly to the radiated fields. It was concluded that a single U-slot rectangular patch on a single-layer substrate with relative permittivity of 4.4 and loss tangent of 0.02 will result in a highly radiating structure.

It is the aim of this paper to expand on these recent studies [5-8] and to find the ideal excitation feed to excite the highly radiating structure of the U-slot rectangular patch on $\varepsilon_r = 4.4$ substrate to achieve the most radiation and impedance bandwidth. TCM will be utilized once more to analyze some of the different excitation feeds found in the literature [9] to determine the least reactive excitation feed structure, which will excite the modes contributing to the optimum resonant behavior of the U-slot patch antenna.

II. MODAL ANALYSIS OF EXCITATION FEEDS FOR U-SLOT PATCH ANTENNA

Modal significance is defined as the normalized amplitude of the characteristic modes. Modes where the modal significance is close to 1 indicate that they contribute significantly to radiation, whereas modes with modal significance close to 0 indicate they do not [4]. Therefore, modal significance gives the antenna designer physical insight on the resonant behavior of an antenna structure independent of the source excitation.

Before we model the highly radiating structure of U-slot patch and $\varepsilon_r = 4.4$ substrate with an excitation feed, we need to first investigate which eigenmodes are resonating on this structure. In Fig. 1, the modal significance of the top 6 significant eigenmodes is shown. It is shown that modes 1, 3, and 4 contribute the most to radiation since their modal significance is close to 1 over the frequency range 2.5-8.5 GHz. Higher order modes 5 and 6 contribute minimally in the higher frequencies. So, prospective excitation sources will aim to excite all or some of the resonating eigenmodes (1, 3, and 4) in the antenna structure.

Figure 2 shows the characteristic currents for modes 1, 3, and 4 at 5.0 GHz. The location of maximum current distribution, where it is desirable to excite the patch, is denoted by the concentrated red color in Fig. 2. The common location for maximum current distribution between all three modes is marked by the dotted black circles in Fig. 2 and is found to be at the base of the U-slot and the inner edge of the U-slot arm.
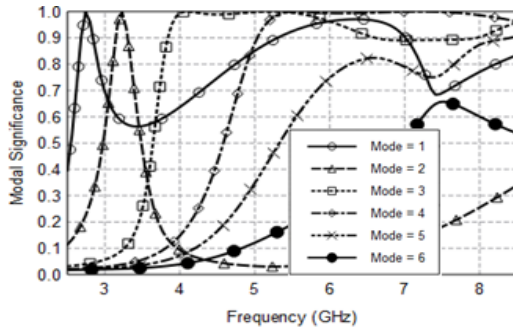

Fig. 1. Modal significance for U-slot patch antenna with $\varepsilon_r = 4.4$ substrate.
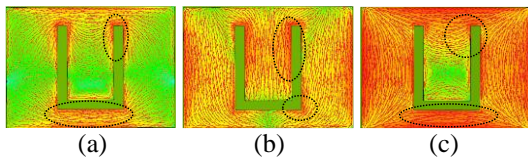

Fig. 2. Characteristic currents of U-slot rectangular patch antenna on $\varepsilon_r = 4.4$ substrate at 5.0 GHz for: (a) mode 1, (b) mode 3, and (c) mode 4.

To find an ideal source feed which will excite the most modes, modal analysis of the U-slot rectangular patch antenna on the $\varepsilon_r = 4.4$ substrate with $\tan(\delta) = 0.02$ is performed with 3 different probe feeds, namely the conventional vertical probe, the L-probe, and the T-probe, shown in Fig. 3. The U-slot patch antenna and probe dimensions, designed using the method of dimensional invariance [1] for a 3.9 GHz design frequency, are shown in the first three columns in Table 1 for each of the probes. The probe radius is defined as r_p. The x- and y-axis positions of the probe are defined

as x_p and y_p, respectively. The probes are placed at the location of maximum current distribution marked in Fig. 2. The horizontal and vertical arms of the L-probe and T-probe are defined as L_h and L_v, respectively. The horizontal arm of the T-probe is symmetric, i.e., its length on the left side of vertical arm is equal to its length on the right side of vertical arm, which is equal to 3.84 mm.
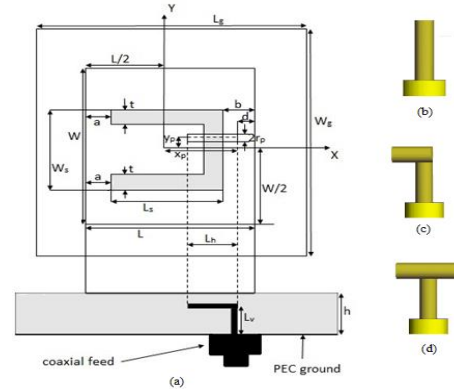

Fig. 3. (a) Geometry of rectangular patch antenna with U-slot, (b) vertical probe, (c) L-probe, and (d) T-probe.

Table 1: U-slot patch antenna dimensions in mm for different feed probe designs

	Vertical Probe (Sim.)	L-Probe (Sim.)	T-Probe (Sim.)	T-Probe (Fabricated)
a	2.25	2.25	2.25	4.38
b	2.25	2.25	2.25	4.38
W	20.25	20.25	20.25	39.48
L	14.62	14.62	14.62	28.51
L_s	10.14	10.14	10.14	19.78
t	1.13	1.13	1.13	2.21
W_s	7.87	7.87	7.87	15.35
W_g	140.17	140.17	140.17	139.41
L_g	134.54	134.54	134.54	128.44
h	7.62	7.62	7.62	15.35
r_p	1	1	1	0.65
x_p	6	4.81	4	10.95
y_p	5	1	1	0
L_h	----	3.84	3.84	2.99x2.28
L_v	7.62	6.53	6.15	12.80
d	1.31	2.5	3.31	3.31

In [8], we performed a modal excitation analysis over the selected frequency range 2.5-8.5 GHz on the U-slot rectangular patch slot and $\varepsilon_r = 4.4$ substrate with vertical probe, L-probe, and T-probe to determine which source feed excites the modes 1, 3, and 4, which contribute to the optimum resonant behavior. It was found that mode 3 is the main mode excited by the conventional vertical probe in the frequency range 2.5-5.7 GHz. Mode 3 is the main mode excited by the

L-probe in the frequency range 2.5-6.1 GHz. Modes 3, 4, and 6 are the main modes excited by the T-probe in the frequency range 2.5-7.0 GHz. Consequently, the T-probe excites the most number of modes over the largest frequency range, and hence, is expected to achieve the highest impedance bandwidth.

In Fig. 4, the modal significance of each of the three probes is shown. The non-excited probe structures are modeled independent of the other antenna elements, i.e., the U-slot patch, substrate, and ground plane. For the vertical probe, in Fig. 4 (a), mode 1 is the contributing mode maxing out at modal significance equal to 0.08. For the L-probe, in Fig. 4 (b), mode 1 is the contributing mode maxing out at modal significance close to 0.16. For the T-probe, in Fig. 4 (c), modes 1 and 2 are the contributing modes maxing out at modal significance close to 0.20. Compared to the other two probes, the T-probe has more modes with higher modal significance which indicates that it is the least reactive feeding structure. This is a desirable feeding structure feature and also explains why the T-probe is expected to achieve the highest impedance bandwidth. The fact that the modal significance of all the probes is relatively low at less than 0.20 indicates that they will not contribute much to the radiation of the entire antenna, which is another desirable feature in feeding structures.
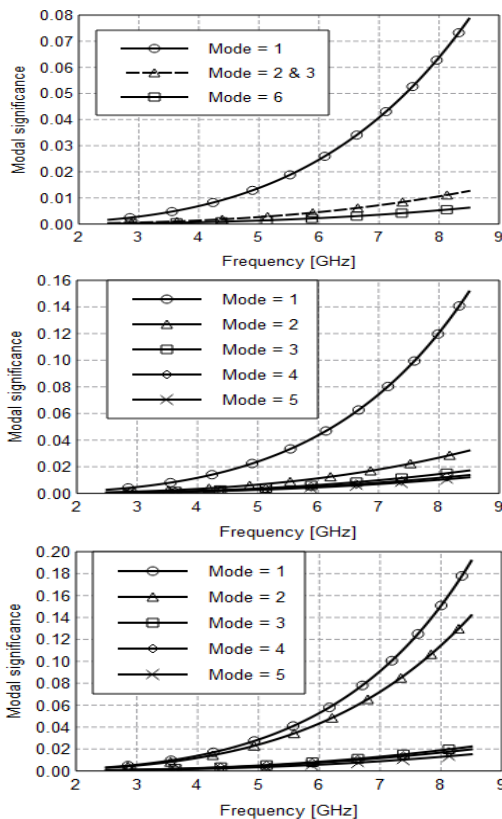

Fig. 4. Modal significance of different excitation feeds: (a) vertical probe, (b) L-probe, and (c) T-probe.

III. OPTIMIZED IMPEDANCE BANDWIDTH OF U-SLOT PATCH ANTENNA

Figure 5 shows the VSWR ≤ 2 bandwidth for the 3.9 GHz U-slot patch design with 3 different probes (dimensions shown in the first three columns of Table 1). Results from two electromagnetic solvers, namely FEKO FEM and HFSS FEM, are shown for validation purposes. The vertical probe in Fig. 5 (a) shows VSWR ≤ 2 bandwidth of 21% between 3.55 GHz and 4.38 GHz. The L-probe feed in Fig. 5 (b) shows VSWR ≤ 2 bandwidth of 82% between 2.74 GHz and 6.58 GHz, and the T-probe feed in Fig. 5 (c) shows VSWR ≤ 2 bandwidth of 96% between 2.86 GHz and 8.16 GHz. The simulation results of the two solvers are in good agreement.
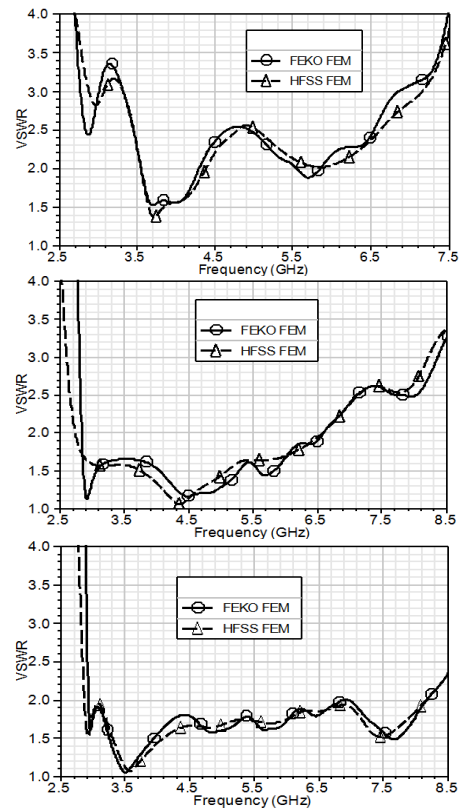

Fig. 5. Simulated VSWR for U-slot patch antenna with different excitation feeds: (a) vertical probe, (b) L-probe, and (c) T-probe.

The small substrate thickness of 7.62 mm used in the T-probe fed antenna design simulation of Fig. 5 (c) was not available for fabrication. Also, the horizontal probe arm of the T-probe was modeled as a rectangular PEC sheet sandwiched between two substrate layers due to lack of proper instrumentation to fabricate a T-shaped probe. Therefore, a bigger patch antenna with thicker multilayered substrate was fabricated for a 2.0 GHz

design frequency, instead. The dimensions of the fabricated T-probe fed U-slot patch antenna are shown in the rightmost fourth column of Table 1. Figure 6 shows the measured and simulated VSWR ≤ 2 bandwidth of the fabricated antenna. As seen in Fig. 6, measured VSWR ≤ 2 bandwidth of over 71% between 1.8 GHz and 3.8 GHz is realized, though bandwidth can be improved between 2.2 and 2.4 GHz. Also, a higher VSWR ≤ 2 bandwidth between 1.8 and 4.8 GHz could be realized if it was not for the oscillations around 2.3, 3.9, and 4.5 GHz. These oscillations are mainly due to the thicker substrate used in fabrication which introduces more surface waves that scatter at substrate edges. The slight discrepancy between the measured and simulated results in Fig. 6 can be attributed to fabrication inaccuracies and manufacturing tolerances, otherwise the pattern demonstrated by the two curves mostly agree.
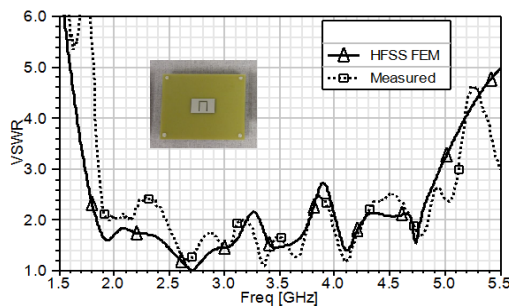

Fig. 6. Measured vs simulated VSWR of fabricated T-probe fed, U-slot microstrip patch antenna with $\varepsilon_r = 4.4$ substrate. Inset: image of fabricated antenna.

IV. CONCLUSION

In this paper, the Theory of Characteristic Modes has been used to find the ideal excitation feed to excite the highly radiating structure of the U-slot rectangular patch on $\varepsilon_r = 4.4$ substrate to achieve the most radiation and impedance bandwidth. Different excitation feeds, namely the vertical probe, L-probe, and T-probe were analyzed to determine the least reactive excitation feed structure, which will excite the modes contributing to the optimum resonant behavior of the U-slot patch antenna. Simulated and experimental results show that a single T-probe feed excites the most number of modes and achieves impedance bandwidth in excess of 70%.

REFERENCES

[1] V. Natarajan and D. Chatterjee, "Comparative evaluation of some empirical design techniques for CAD optimization of wideband U-Slot microstrip antennas," *Applied Computational Electromagnetics Society (ACES) Journal*, vol. 20, no. 1, pp. 50-69, March 2005.

[2] G. Rafi, and L. Shafai, "Broadband microstrip patch antenna with V-slot," *IEE Proceedings Microwaves Antennas and Propagation*, vol. 151, no. 5, pp. 435-440, 2004.

[3] R. F. Harrington and J. R. Mautz, "Theory of characteristic modes for conducting bodies," *IEEE Trans. Antennas Propag.*, vol. AP-19, no. 5, pp. 622–628, Sept. 1971.

[4] M. Vogel, G. Gampala, D. Ludick, U. Jakobus, and C.J. Reddy, "Characteristic mode analysis: putting physics back into simulation," *IEEE Antennas Propag. Mag.*, vol. 57, no. 2, pp. 307-317, Apr. 2015.

[5] M. M. Elsewe and D. Chatterjee, "Modal analysis of patch slot designs in microstrip patch antennas," *2016 IEEE International Conference on Wireless Information Technology and Systems (ICWITS) and Applied Computational Electromagnetics (ACES)*, Honolulu, HI, March 13-17, 2016.

[6] M. M. Elsewe and D. Chatterjee, "Modal analysis of substrate permittivities in microstrip patch antennas," *2016 IEEE International Conference on Wireless Information Technology and Systems (ICWITS) and Applied Computational Electromagnetics (ACES)*, Honolulu, HI, March 13-17, 2016.

[7] M. M. Elsewe and D. Chatterjee, "Characteristic mode analysis of ground plane size in microstrip patch antennas," *2016 IEEE International Symposium on Antennas and Propagation & USNC/URSI National Radio Science Meeting*, Fajardo, Puerto Rico, June 26-July 1, 2016.

[8] M. M. Elsewe and D. Chatterjee, "Characteristic mode analysis of excitation feed probes in microstrip patch antennas," *2016 IEEE International Symposium on Antennas and Propagation & USNC/URSI National Radio Science Meeting*, Fajardo, Puerto Rico, June 26-July 1, 2016.

[9] C.L. Mak, K.F. Lee, and K.M. Luk, "Broadband patch antenna with a T-shaped probe," *IEE Proceedings Microwaves Antennas and Propagation*, vol. 147, no. 2, pp. 73-76, 2000.